RICE UNIVERSITY

Optimizing Magnetic Iron Oxide Nanoparticles for Cancer Theranostic Applications

By

YU YIN

A THESIS SUBMITTED
IN PARTIAL FULFILLMENT OF THE
REQUIREMENTS FOR THE DEGREE

Master of Science

APPROVED, THESIS COMMITTEE

Gang Bao
Foyt Family Professor, Bioengineering
Professor, Chemistry
CPRIT Scholar in Cancer Research
Associate Dean, Research and Innovation

Qingbo Zhang
Assistant Research Professor,
Bioengineering

Jun Lou
Professor, Materials Science and NanoEngineering
Associate Chair, Materials Science and
NanoEngineering

HOUSTON, TEXAS

June 2020

RICE UNIVERSITY

Optimizing Magnetic Iron Oxide Nanoparticles for Cancer Theranostic Applications

by

YU YIN

A THESIS SUBMITTED
IN PARTIAL FULFILLMENT OF THE
REQUIREMENTS FOR THE DEGREE

MASTER OF SCIENCE IN BIOENGINEERING

APPROVED, THESIS COMMITTEE

Dr. Gang Bao, Chair
Foyt Family Professor, Bioengineering
Professor, Chemistry
CPRIT Scholar in Cancer Research
Associate Dean, Research and Innovation

Dr. Qingbo Zhang
Assistant Research Professor,
Bioengineering

Dr. Jun Lou
Professor, Materials Science and
NanoEngineering
Associate Chair, Department of Materials
Science and NanoEngineering

HOUSTON, TEXAS
June 2020

ABSTRACT

Optimizing Magnetic Iron Oxide Nanoparticles for Cancer Theranostic Applications

by

Yu Yin

Magnetic iron oxide nanoparticles (MIONs) have unique physical-chemical properties for a wide range of biomedical applications, including targeted drug delivery, multimodality molecular imaging, thermal therapies, and biomarker detection. In this study, I optimized MIONs for different biomedical applications. First, to improve the efficacy of cancer immunotherapy for solid tumors, I increased endocytosis of MIONs into T cells using cell penetrating peptides to enable better *in vivo* imaging and targeting. Secondly, to facilitate hyperthermia therapy and anti-cancer drug delivery by heat-triggered release, I coated MIONs with mesoporous silica and demonstrated enhanced colloidal stability and heating efficiency. Thirdly, to measure the levels of trace biomarkers for early cancer detection with high sensitivity, I quantified pancreatic cancer biomarkers in patient serum samples using europium-doped iron oxide nanoparticle-linked immunosorbent assay (ILISA) and optimized the detection limit of the assay. Our work further expanded the translational potentials of MIONs.

Acknowledgments

First, I would like to express my sincere gratitude to Dr. Gang Bao, for your immense guidance and support. I am forever grateful for your mentorship not only for rigorous, independent, and high-standard scientific research, but also for the times that you earnestly admonished me to reflect about what my goals are and to introspect what kind of person I want to become.

Thank you, Dr. Qingbo Zhang, for your patient guidance, generous help, and expertise in chemistry. Even though it has been less than a year since you joined the lab, I have learned a lot from you.

I would like to thank Dr. Jun Lou tremendously for your timely support and for your expertise in materials science and nanoengineering.

I would want to say thank-you to all current and alumni lab members. I wholeheartedly thank Dr. Linlin Zhang, for being sincerely caring to me, for the knowledge you taught me and for the extensive time dedicated to helping me with my projects. Many thanks to Amy Tang for all your tremendous support, trust, and the honor for me to be one of your bridesmaids. Thank you, Dr. Yidan Pan, for your gourmet foods and a lot of conversations as food for thought; Dr. Julie Park, Kevin Li and Kaiyi Jiang

for all your intellectual stimulations, and motivations for me to emulate you both for research and in life; Dr. Sheng Tong for your insightful guidance; Daniel Torres Hinojosa for all the technological support; Harsha Deshmukh for your excellent organization and management of the lab; Dr. Buhle Moyo, Lucas Brown, Tim Davis, BY Yoo, Mithil Chokshi, for together fostering an air of community and camaraderie.

I would like to acknowledge the Rice Shared Equipment Authority (SEA) Team, especially Dr. Wenhua Guo for TEM imaging, Dr. Jianhua Li for XRD measurements and Dr. Christopher Pennington's assistance for ICP-MS. I would like to also acknowledge Houston Methodist for its MRI facility. We thank collaborators at MD Anderson Cancer Center, Dr. Anirban Mitra for providing patient serum samples, and Dr. Cassian Yee for providing T cell samples.

And lastly, I am forever most grateful for my parents for your unconditional and steadfast love and support, believing in me through all my ups and downs. Without you none of this would have been possible.

This research is funded by the Cancer Prevention and Research Institute of Texas (CPRIT RR140081 to G.B.).

Content

List of Figures

List of Tables

List of Equations

Chapter 1 Introduction and Background

I. Magnetic Iron Oxide Nanoparticles (MIONs)

Magnetic iron oxide nanoparticles (MIONs) refer to a category of materials consisting of magnetite (Fe_3O_4) or maghemite (γ- Fe_2O_3) nanocrystals and can be synthesized to be of various sizes. MIONs have unique physical-chemical properties and have been receiving tremendous research interests for developing versatile and promising biomedical applications, including controlled and targeted drug and gene delivery, multimodality molecular imaging, thermal therapies, and biomarker detection[1] (Figure 1) .

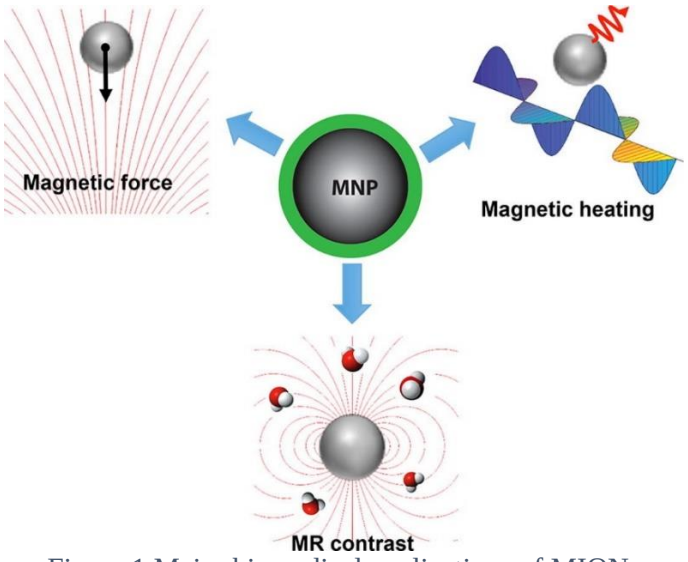

Figure 1 Major biomedical applications of MIONs

Based on the magnetic properties of MIONs, three major biomedical applications have been developed[1]. Magnetic force can be generated by MIONs experiencing a magnetic field gradient. Magnetic resonance (MR) contrast results from the effect of MIONs on the relaxation of water protons. Magnetic heating can be triggered by MIONs in an alternating magnetic field.

MIONs are prepared by two major chemical methods[2,3]. The conventional synthesis method is by co-precipitation of stoichiometrically mixed Fe^{2+} (ferrous) and Fe^{3+} (ferric) ions in an alkaline solution. The advantage of this method is that it can be easily scaled up for mass production of the MIONs. However, the drawback is that it is arduous to obtain uniform iron oxide core sizes with narrow size distributions and hence controlled magnetic properties[2,3]. In contrast, thermal decomposition of organic complexes of iron in the presence of capping agents (e.g. oleic acid and oleyl amine), can provide excellent control over the size, shape and monodispersity of the MIONs with desired magnetic properties[4]. Due to the usage of organic solvent, it requires further surface modifications to render the as-synthesized MIONs water-dispersible and biocompatible[5,6].

The unique structure-property relationship of MIONs is largely size-dependent (Figure 2) and nanoparticles behave differently from their bulk materials. MIONs with the size less than 100 nm typically consist of a single magnetic domain per magnetic particle with the magnetic moment from all unpaired electrons aligned[7]. Due to thermal fluctuation, the magnetic moment randomly flips among several crystal axes of the nanoparticle. The typical time between two flips is called the Néel relaxation time. When the particle size is sufficiently small, the time used to measure the magnetization

of the nanoparticles is much longer than the Néel relaxation time. Thus, their magnetization appears to be in average zero. The magnetic nanoparticles are superparamagnetic. Superparamagnetic iron oxide nanoparticles (SPIONs) become magnetized up to their saturation magnetization. Upon removal of the magnetic field, they no longer exhibit any residual interparticle magnetic interaction[7]. This property is crucial for maintaining nanoparticle colloidal stability and help prevents nanoparticle aggregation.

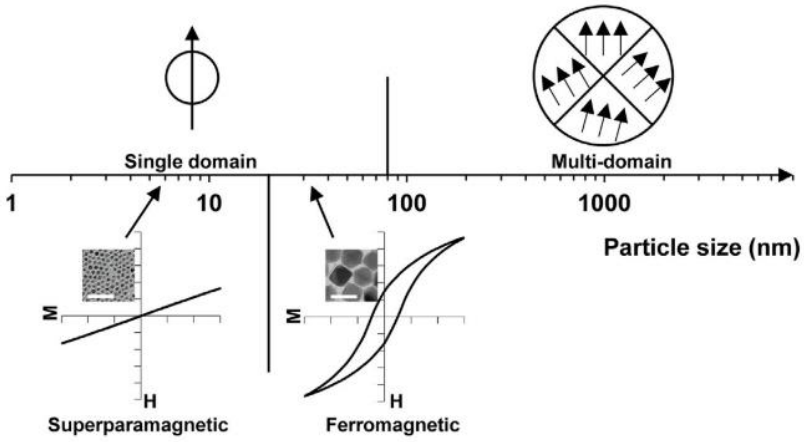

Figure 2 Size-dependent properties of MIONs

Larger MIONs contains multiple magnetic domains while smaller MIONs with single domain change from ferromagnetic to superparamagnetic as the size decreases to about 25 nm[1]. (Inserts are TEM images and hysteresis curves of 6-nm and 33-nm MIONs, respectively[4].)

II. MIONs for Cancer Theranostic Applications

1.2.1 MIONs for cell imaging and tracking

Superparamagnetic iron oxide nanoparticles (SPIONs) can serve as either a T_1 or a T_2 contrast agent for magnetic resonance imaging (MRI)[8,9] and as tracers for magnetic particle imaging (MPI)[10]. In MRI, a radio

frequency pulse is applied to excite the protons mainly from water. Then excited hydrogen atoms will return to the equilibrium state via two relaxation processes, longitudinal (spin–lattice) relaxation T_1 and transverse (spin–spin) relaxation T_2. The relaxation processes yield the MR image contrast and can be adjusted to contrast different tissues. The presence of MIONs generates a local magnetic field that alters the relaxation of the surrounding water protons. Commonly MIONs provide T_2 contrast by appearing to be dark spots in T_2-weighted images owing to their gigantic magnetic moment that accelerates the decay of the transverse magnetization of water protons. T_2 relaxivity (R_2) is defined as the reciprocal of T_2 ($1/T_2$). The signal intensity and imaging contrast are closely related to the proton density of the tissue being imaged as well as the magnetization properties, size, and surface coating[11]. To achieve higher saturation magnetization that are desirable for magnetic heating and magnetic resonance imaging, researchers have also been doping other elements, such as cobalt, manganese and zinc, into the iron oxide nanoparticles[12,13]. Incorporating other components into MIONs may induce safety concerns and thus these MION formulations requires rigorous examinations of their toxicity and biocompatibility for biomedical applications. Proper surface modifications such as PEG coating[5] not only improves biocompatibility, but also offer the

potential to further functionalize the nanoparticles for multimodal imaging integrating both MRI and fluorescent imaging[14–16].

Biosafety of MIONs synthesized and surface modified by various methods has been extensively investigated in different animal models and results have proved that MIONs are in general safe and biocompatible when using reasonable concentration range[17–20]. Endocytosis of MIONs are dependent on a myriad of parameters such as the size, shape, and stiffness of nanoparticles, the surface charge types, ligands and other modifications on the nanoparticles, the biomechanical properties of the cell membrane, as well as the local environment of the cells[21]. At cellular level, researches have shown that endocytosed MIONs localize to the lysosomal compartment after *in vitro* incubation[22]. After intravenous injection, the majority of MIONs are cleared by the reticuloendothelial system (RES) encompassing mainly monocytes of the blood, macrophages, lymphoid organs (lymph nodes, spleen), and liver[23]. To maintain iron homeostasis, the body gradually incorporates the iron in circulation that is metabolized from the biodegradable MIONs into hemoglobin of erythrocytes[23].

Several MION-based formulations have been approved by the U.S. Food and Drug Administration (FDA) for human use or undergoing clinical trials[24], such as Feridex® (ferumoxides) (dextran-coated MIONs) as a

imaging contrast agent for the detection of liver lesions[25]. MIONs, especially those with active targeting molecules, such as monoclonal antibody specific to certain tumor types and folic acid, have also been employed to image and diagnose tumors[26–29]. However, there has long been controversy of enhanced permeation and retention (EPR) effect for nanomaterials. It has been reported that based on literature survey from the past decades, only 0.7% (median) of nanoparticles (NPs) via intravenous/systemic injection reached the tumor site[30], and that nanoparticles targeting solid tumor sites have to complete transcytosis across endothelium to solid tumors, instead of EPR[31,32]. MION designs need to be further optimized for improved pharmacokinetics to enable the targeted delivery of a larger dose to the tumor site to improve the therapeutic efficacy while reducing systemic toxicity and/or offer better imaging signals.

Cell therapies are promising strategies in addressing repairing and regeneration of tissues and immune therapies. It is crucial to understand and control the trafficking and localization of the therapeutic cell products for improving the efficacy and monitoring the treatment process. Given that MIONs present excellent MRI imaging capability, they have been extensively investigated for cell tracking by direct labeling[33]. Cells can be directly and indirectly labeled. Direct labelling refers to methods that

imaging agents are directly loaded into therapeutic cells; and indirect labelling usually requires genetic modifications of the therapeutic cells to express a reporter gene product to enable imaging. MRI is advantageous in that it can provide non-invasive and real-time imaging for cell tracking at any tissue depth with excellent soft tissue contrast. There is also no ionizing effect as in computer tomography (CT) or positron emission tomography (PET). Typical clinical magnetic resonance imaging scanners are with a magnetic field strength up to 7 Tesla that has no evident adverse effect to the human body and the magnetic field is not attenuated by the tissue.

T cells play the essential role in combatting tumor and the tracking of T cells using MIONs have done by several groups[34–43]. Information about macrophages[44,45], dendritic cells[46] and other immune cell types has also been revolutionizing our insights about the immune system and immunotherapies. In addition, progenitor or stem cells transplantation tracking have been helpful for regenerative medicine applications[47–52].

1.2.2 MIONs for magnetic targeting

MIONs can be manipulated by magnetic force generated by magnetic field gradient:

Equation 1 Magnetic force

$$\vec{F}_M = (\vec{m}\cdot\nabla)\,\vec{B} \tag{1}$$

The magnetic moment of the particle is determined by

Equation 2 Magnetic moment

$$\vec{m} = \rho V \vec{M} \tag{2}$$

where ρ is particle density, V is volume of magnetic material in the particle and $\boldsymbol{M}$ refers the magnetization of the particle.

MIONs in biological fluids will also experience the Stokes' drag force in the opposite direction of the magnetic force on the particle:

Equation 3 Stokes' drag force

$$\mathbf{F}_d = 6\pi\,\eta\,R\,v \tag{3}$$

In this equation, η is the fluid viscosity, R is the hydrodynamic radius of the particle, and v is the velocity of the particle.

Magnetic targeting using MIONs have been developed for optimizing drug biodistribution and gene delivery[53,54]. There are numerous physiological barriers to drug and gene delivery, such as the extracellular matrix and the vascular endothelium. Novel approaches enhancing vascular permeability temporarily will greatly improve drug transport across the endothelial barrier for better therapeutic efficacy. A promising method has been proposed to disrupt endothelial junctions using magnetic force generated by endocytosed MIONs[55]. Besides, the magnetic nanoparticle-baculovirus hybrid system has been designed for magnetically controllable

in vivo genome editing with precise activation of CRISPR-Cas9 only in the target tissue helps to reduce genotoxicity[56]. Magnetic force can also be employed for magnetic purification of molecules and cells[57].

The efficacy of cell therapies largely dependent on adequate amounts of functional cells engaged at the diseased sites. Therefore, it is attractive to remotely control cell mechanics and manipulate cell migration by magnetic targeting for stem cell therapy[58] and immunotherapy[59].

1.2.3 MIONs for magnetic heating

Under an alternating magnetic field (AMF), MIONs of multidomain ferro- or ferri-magnetic size range dissipate heat because of the hysteresis losses during relaxation. The heating efficiency of MIONs is characterized by specific absorbed rate (SAR). A modified dynamic hysteresis model based on the conventional linear theory of magnetic fluid heating (MFH)[60] indicated that the heating efficiency of MIONs increased with size and the 40 nm ferromagnetic nanoparticles possess an approximate theoretical limit of the SAR value under a clinically relevant AMF[4]. SAR is calculated with the following equation:

Equation 4 Specific absorbed rate

$$\mathrm{SAR} = \frac{1}{m_{\mathrm{Fe}}} C_{\mathrm{sol}} m_{\mathrm{sol}} \left(\frac{\mathrm{d}T}{\mathrm{d}t} \right) \tag{4}$$

where m_{Fe} is the mass of the iron in the sample, C_{sol} is the specific heat of the solvent, m_{sol} is the mass of the solvent, and dT/dt is the slope of the temperature *versus* time.

Major Parameters Effecting Magnetic Nanoparticle Heating in an Alternating Magnetic Field		
Nanoparticle	**Medium/Solvent**	**Magnetic Field**
• Saturation Magnetization • Magnetic Anisotropy • Size • Polydispersity • Aggregation • Coating • Oxidation	• Nanoparticle Concentration • Viscosity • Specific Heat	• Field Strength • Frequency • Uniformity

Table 1 Major Parameters Effecting Magnetic Nanoparticle Heating in AMF

Summary of important parameters for SAR calculation and prediction for magnetic nanoparticle heating applications (adopted from Ref[61]).

Hyperthermia therapy (HT) refers to the treatment of disease through heating to a temperature generally over 42℃ above the tissue tolerance. MIONs can be locally injected to the solid tumor sites or endocytosed by relevant immune or cancer cells to generate heat within the confined region of the diseased tissues while sparing the surrounding healthy tissues. Taking advantage of the heating properties of MIONs, researchers have utilized MIONs for magnetic heating and have demonstrated that HT works in synergy with chemotherapy, radiotherapy and/or immunotherapy for various types of cancers[62–64], especially for brain tumors[65].

Although magnetic heating by MIONs is promising, there remains a few technical difficulties for translating magnetic heating to clinics. First, the human body-size inductive coil generating an AMF of high strength and high frequency is costly and requires compatible cooling system. High frequency ($f > 10^6$ Hz) can also induce eddy currents and thus nonspecific heating of the tissue in the body fluid, which can be a safety concern. Secondly, there is also a need of accurate thermometry within the tumor mass and more precise tumor heating. It also warrants more thorough investigation into the mechanisms of hyperthermia, especially its immunogenic effect.

Magnetic heating can also be applied for localized heat-triggered release of anticancer drugs loaded onto modified MIONs. The switch between the ON and OFF states of the AMF can mediate the temporally controlled release of drugs as well.

1.2.4 MIONs for cancer biomarker detection and screening

The early detection of cancer allows more opportunities for effective treatments and can significantly improve patient survival rate. Therefore, it is valuable to develop biotechnologies that can detect early signs of the disease, or even provide large scale screening capability for populations with high risks of having tumors. Cancer biomarkers can be referred to a broad

range of biochemical entities, such as nucleic acids, proteins and glycoproteins, small metabolites, as well as circulating tumor cells found in the circulation[66]. Quantifying certain biomarkers in oncology can play a critical role in facilitating diagnosis, evaluating treatment efficacy, assessing patient prognosis, monitoring risk of tumor recurrence and so on.

As early as in 1965, Dr. Joseph Gold first reported the elevated existence of tumor-specific antigens in colonic carcinoma samples compared with normal ones, and named it carcinoembryonic antigen (CEA)[67]. Later, several other serum biomarker tests were developed for a variety of cancers, including CA19-9 for colorectal[68] and pancreatic cancer[69], CA15-3 for breast cancer and CA125 for ovarian cancer[66]. However, these biomarkers are not specific for a single cancer. For example, CEA level often elevates in patients with lung or breast cancer, and CA-125 can be high in women with noncancerous gynecological conditions[70]. Nevertheless, one of the most commonly used and reliable biomarker for prostate cancer recurrence or as an indicator of treatment efficacy (instead of early disease detection) is the serum prostate-specific antigen (PSA)[71].

Immunohistochemistry is conventional in biomarker detection. This technology requires invasive biopsy and staining of histological specimens for one or multiple markers. Besides, due to the heterogeneity nature of

biological tissues, the small amount of tissues from biopsy may not be truly representative. In contrast, enzyme-linked immunosorbent assay (ELISA) is a high-throughput platform technique that can sensitively quantify the amount of analyte present in a physiological fluid such as serum or urine. Despite these advantages of ELISA, this technology is intrinsically unstable due to the enzymatic reactions for signal amplification and calibrations must be conducted every time before each measurement. To this end and to further optimize the detection limit, our lab has previously established an upgraded platform technology called iron oxide nanoparticle linked immunosorbent assay (ILISA) technology[72,73] (Figure 3).

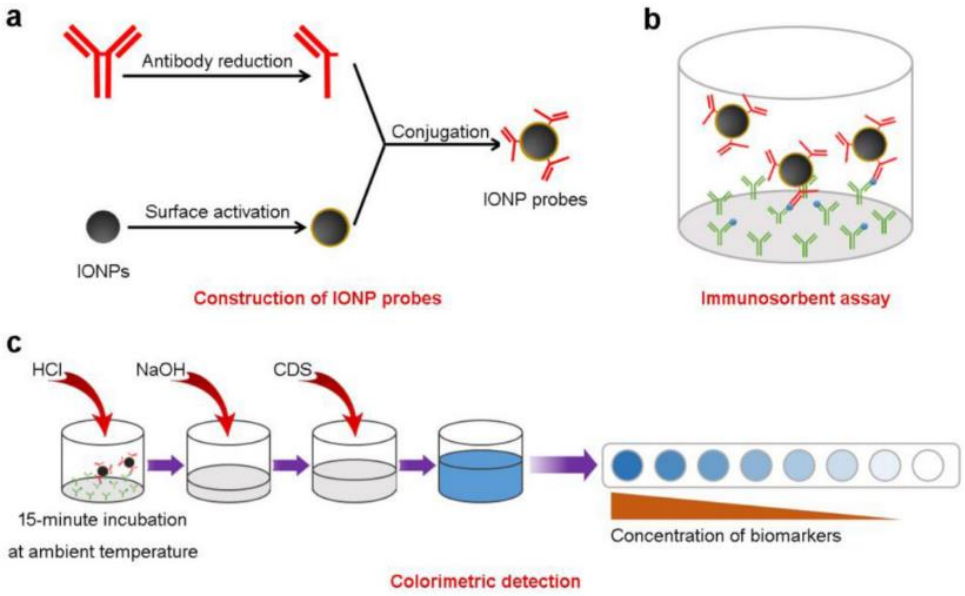

Figure 3 Scheme of the iron oxide nanoparticle linked immunosorbent assay (ILISA)

ILISA[73]: (a) Detection probes are constructed by conjugating IONPs with fragmented antibodies. (b) The samples containing target molecules are incubated with capture antibodies immobilized on to a solid support. Surface bound target molecules are detected with the IONP probes. (c) The probes bound to the target molecules were measured using a colorimetric assay. CDS, color development solution.

In this sandwich assay, MIONs with surface modification bind to immobilized target molecules captured by the capturing antibodies coated on the plate and are then dissolved by acids into individual metal ions for quantification by a stable chromogenic reaction[72]. By this mean, the detection sensitivity of ILISA rely on the number of iron atoms in each MION, i.e., the size of the iron oxide nanocrystal in a probe. We have shown that ILISA can achieve sub-picomolar detection sensitivity for four important serological markers, IgA, IgG, IgM, and C-reactive protein (CRP), and that levels of all four markers in normal sera, simulated disease-state sera and the serum samples from patients infected with West Nile virus (WNV) or human herpes virus (HHV) can be accurately quantified over a large dynamic range.

Chapter 2 To improve the efficacy of CAR T cell therapy to solid tumors

2.1 Introduction

Immunotherapy is the treatment harnessing the patient's own immune system to help the body combat cancer. One of the most promising clinical advancements is the development of adoptive cell therapy (ACT)[74]. The patient's autologous T cells can be collected from tumor site to be activated tumor-infiltrating lymphocytes (TIL)[75], or collected from the blood to be modified on natural T cell receptors (TCR)[76], or genetically engineered with artificial chimeric antigen receptors (CAR)[77] (Figure 4). The empowered T cells are further expanded *ex vivo* and back infused to the body to kill cancer cells more specifically and efficiently. FDA approved two CAR T therapies both targeting CD-19 on the surface of cancerous B cells for blood cancers in 2017, Kymriah (tisagenlecleucel) for certain pediatric and young adult patients with a form of acute lymphoblastic leukemia (ALL)[78] and Yescarta (axicabtagene ciloleucel) for the treatment of adult patients with relapsed or refractory large B-cell lymphoma[79].

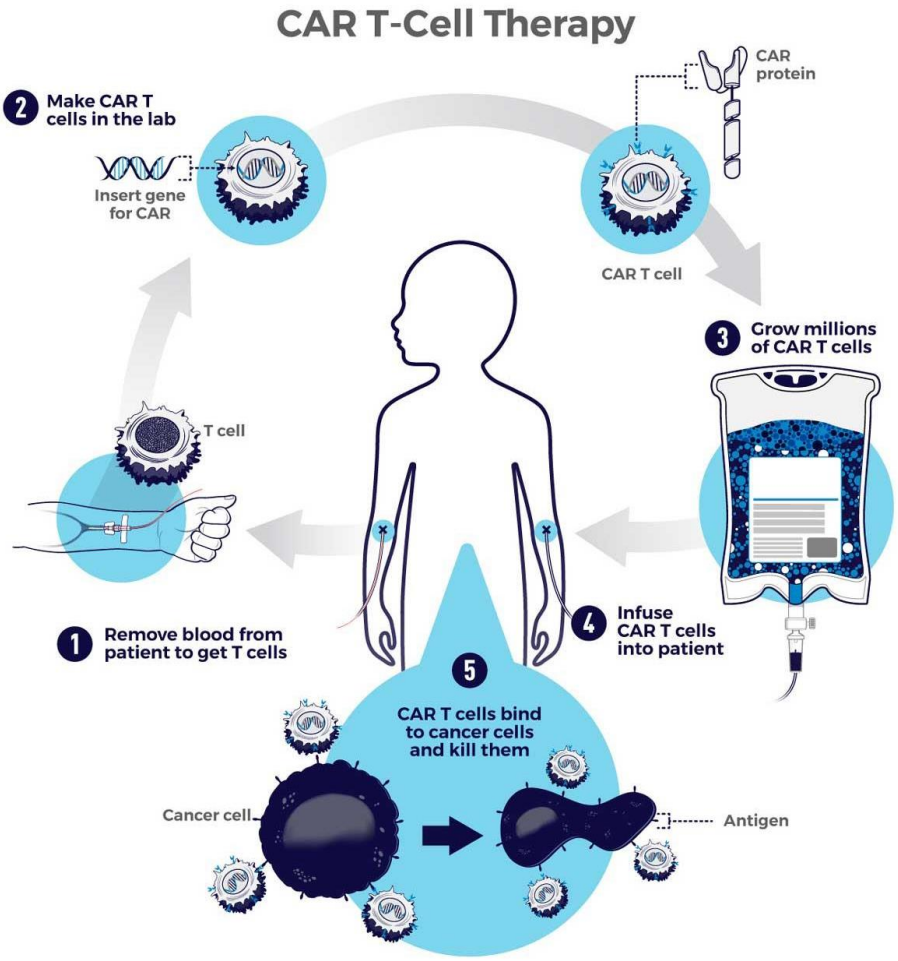

Figure 4 Illustration of the steps for creating CAR T-cell therapy

CAR T-cell therapy[77]: Step 1 – Remove blood from patient to get T cells. Step 2 – Make CAR T cells in the lab. Step 3 – Grow millions of CAR T cells. Step 4 – Infuse CAR T cells into patient. Step 5 – CAR T cells bind to cancer cells and kill them.

Despite these remarkable successes of ACT, several challenges remained to be addressed. Two major issues are that: first, activated T cell expansion in circulation can cause autoimmune diseases and cytokine release syndrome that can be lethal; secondly, due to antigenic heterogeneity and immunosuppressive tumor microenvironment, ACT for solid tumors represents an unmet clinical need. An essential theme of the ACT for

treating solid tumors is the importance of localization. The efficacy of the therapy and patient prognosis are highly related to the ability of the therapeutic cells to reach and be retained at a specific anatomical site. To achieve this site-specific localization, researchers have investigated strategies such as locoregional injections and enhancing intrinsic cell homing mechanisms. Nevertheless, it would still be beneficial to manipulate cell localization with external and non-invasive control to increase the portion of functional therapeutic cells at the solid tumor sites to improve the efficacy of ACTs. One of the promising modalities to realize this goal is by magnetic targeting.

These challenges motivate us to not only boost cancer immunotherapy but also reduce severe side effects. We strive to have a clearer understanding of how adoptive transferred T cells behave *in vivo*. Thus, we want to non-invasively track the migration, biodistribution, viability, and functionality of different T cell populations. And we also aim to enhance trafficking of functional T cells to the tumor sites and retain them to their therapeutic sites.

In this section, we first sought to find the exquisite balance between (a) unaltered cellular viability and biological functions after cellular uptake of MIONs, and (b) adequate magnetic responsiveness. Next, we aimed to image cells loaded with MIONs using magnetic resonance imaging (MRI)

and intravital fluorescence imaging for tracking purpose. Then we sought to prove that cells loaded with MIONs can be manipulated with magnetic field for site-specific targeting.

2.2 To Identify the Optimal MION Formulations and T Cell Loading Conditions

2.2.1 Materials and Methods

MIONs of 15nm diameter were synthesized by thermodecomposition of iron acetylacetonate and seed-mediated growth using an established protocol[4]. Physical properties of the nanoparticles were analyzed by SQUID, TEM, DLS and relaxometer. MIONs were next coated with PEG2K using dual solvent exchange method[5]. With the biocompatible phospholipid-PEG coating on MIONs, a lipophilic fluorophore, DiI (excitation: 520nm; emission: 570nm), can be readily inserted into the lipid-PEG layer for fluorescent signal analysis. To facilitate cellular internalization of nanoparticles for T cells that are non-phagocytic in nature, we conjugated cationic cell penetrating peptides (CPP)[80], TAT[47,81] (in abbreviation of transactivated-transcription) derived from HIV, or polyarginine[82,83], onto the nanoparticles.

For *in vitro* studies, Jurkat cells, which are immortalized human T lymphocytes, were employed as a model cell line of T cell immunology. Genetically modified T cells (GP100 T cells; gift from Dr. Cassian Yee at MD Anderson Cancer Center) were also used for comparison. Cells were cultured in a 24-well plate (500μl per well; N=3) at the density of 2×10^6 cells/ml using RPMI1640 medium (5% FBS + 1% pen-strep + 0.1% IL-2) under 5% CO_2 at 37°C. Cells were collected after incubation with MIONs for 2 hours, 8 hours or 24 hours at an initial Fe concentration of 100μg/ml or 200μg/ml (250μl per well). After centrifugation at 300G for 5 minutes, cell pellets were disturbed using trypsin and washed with 1X PBS three times to remove uninternalized nanoparticles. Cell viability was determined using Trypan blue and BIORAD cell counter. T_2 relaxivity was measured under 0.47T magnetic field strength using a Carr-Purcell-Meiboom-Gill (CPMG) sequence by Minispec. Fluorescent signal was measured by BD C6 Flow Cytometry. Intracellular Fe content was quantified by ferrozine assay[84]. Lysosomes were stained by LysoTracker® and nuclei were stained by Invitrogen Hoechst 33342 nucleic acid stain. Confocal fluorescence imaging was conducted on DeltaVision microscope.

2.2.2 Results and Discussions

2.2.2.1 Characterization of MIONs

We carefully characterized the properties of the as-synthesized nanoparticles. Uniform size ensures uniform property. We confirmed using TEM that the nanoparticles were about 15nm in diameter with a narrow size distribution (15.22 nm ± 1.38nm) (Figure 5).

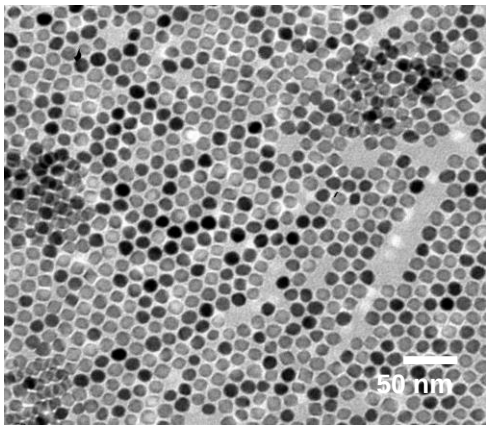

Figure 5 TEM of 15nm MIONs

Next, we characterized the magnetic properties of MIONs. The lack of a hysteresis loop indicated our nanoparticles are superparamagnetic (Figure 6). This property is crucial for desirable dispersity of nanoparticles in aqueous environment.

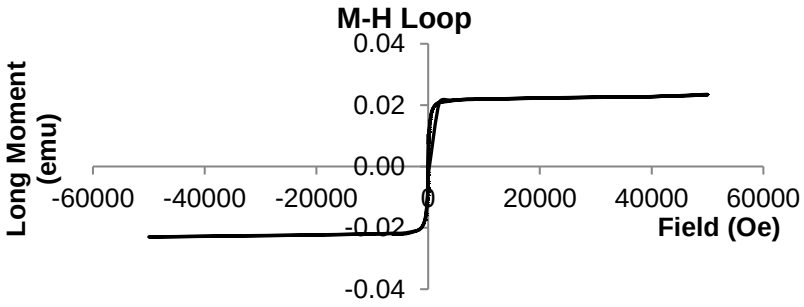

Figure 6 Hysteresis pattern of MIONs measured by SQUID indicated superparamagnetism

Nanoparticles reduced T_2 relaxation time linearly depend on iron concentration, confirming that MIONs can be a good candidate for magnetic resonance imaging (Figure 7).

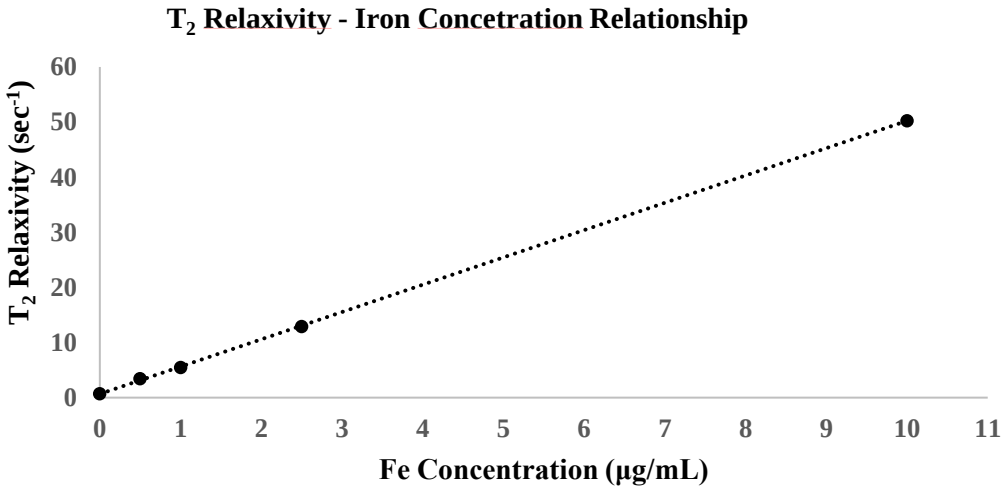

Figure 7 The linear relationship between Fe content and T_2 relaxivity

Stability of nanoparticles is also important for biological applications. We incubated nanoparticles in cell culture medium for over a week at 37°C and did not observe significant changes in nanoparticle sizes. There was no degradation of NPs (Table 2).

	Hydrodynamic Diameter (nm)	Polydispersity (nm)
Before	63.53 ± 0.86	18.13
After	62.53 ± 0.15	17.83

Table 2 Hydrodynamic diameters of NPs before and after incubation in cell culture medium

2.2.2.2 In vitro studies of MIONs cellular uptake

After two hours of incubation, we observed from the flow cytometry data that the percentage of cells with MIONs significantly increased with the conjugation of cell penetrating peptides after 2-hour incubation (Figure 8). Poly-arginine (12-unit) was more efficient than TAT in facilitating endocytosis. Intracellular Fe content was quantified by ferrozine assay to be 1.16 pg/cell. Assuming MIONs are spherical and made of Fe_3O_4 with a density of ρ = 5.17 g/cm^3, we did the calculation to obtain that there were approximately 4.2× 10^4 MIONs per cell. Cell viability was able to be maintained at above 80% after incubation and washing steps for all samples, indicating that there was no observable cytotoxicity of the CPP-conjugated MIONs delivered into cells.

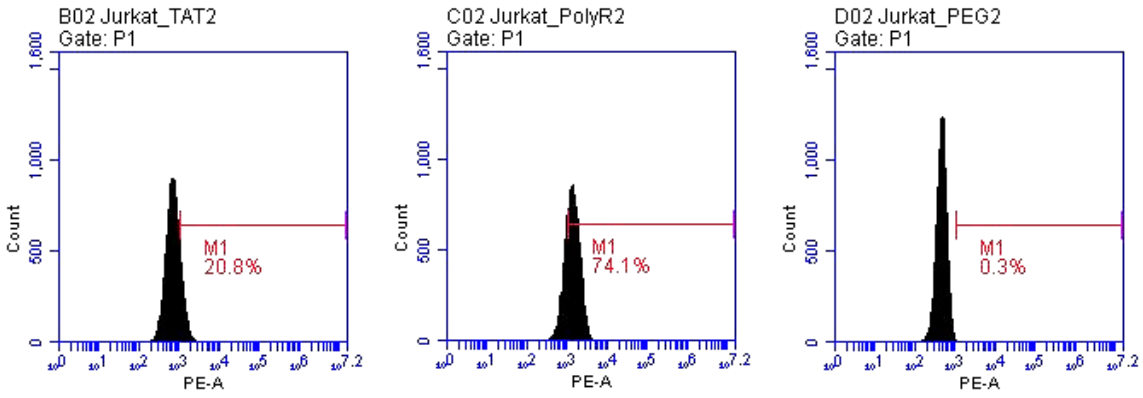

Figure 8 Conjugation of cell penetrating peptide (CPP) improved cellular uptake of MIONs

Then we explored the effect of different conjugation ratios on MION internalization. Take TAT group for example, we observed that cellular

uptake of NPs increased with the conjugation ratio of cell penetrating peptides (Figure 9), with 1:400 close to a plateau (Figure 10).

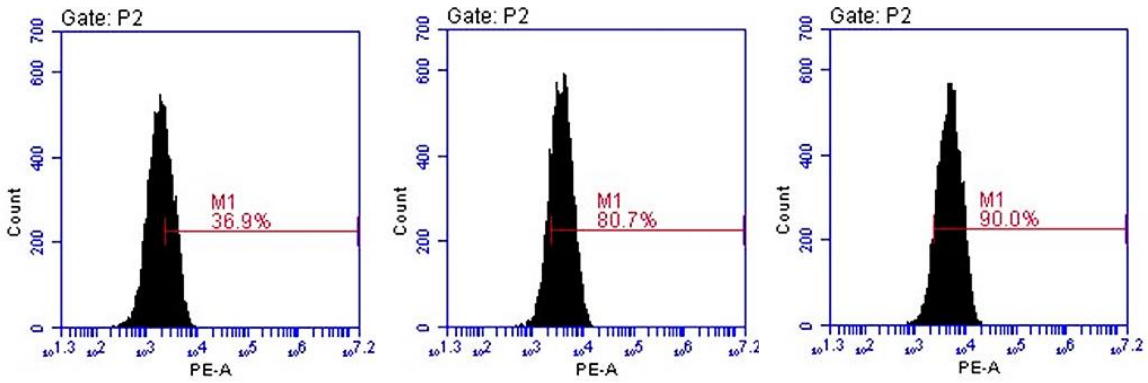

Figure 9 TAT conjugation ratio increased internalization

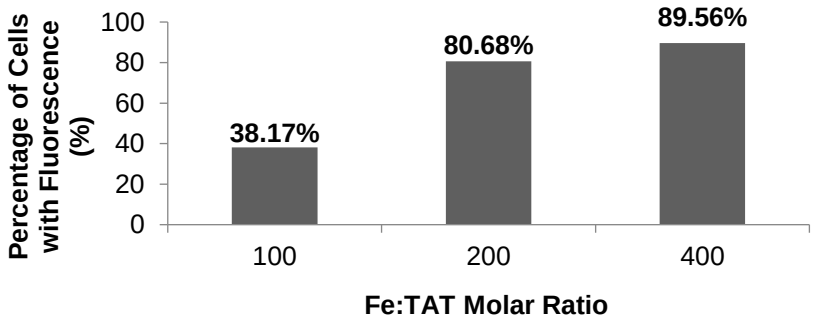

Figure 10 The effect of different conjugation ratios on NP internalization

Internalization of MIONs also increased with MION concentrations. From the diagram on the right in Figure 11, we could differentiate the fluorescence intensity peaks of the two groups with 100 μg/mL and 200 μg/mL concentrations. After 24 hours, almost all cell populations were able to uptake NPs (Figure 11).

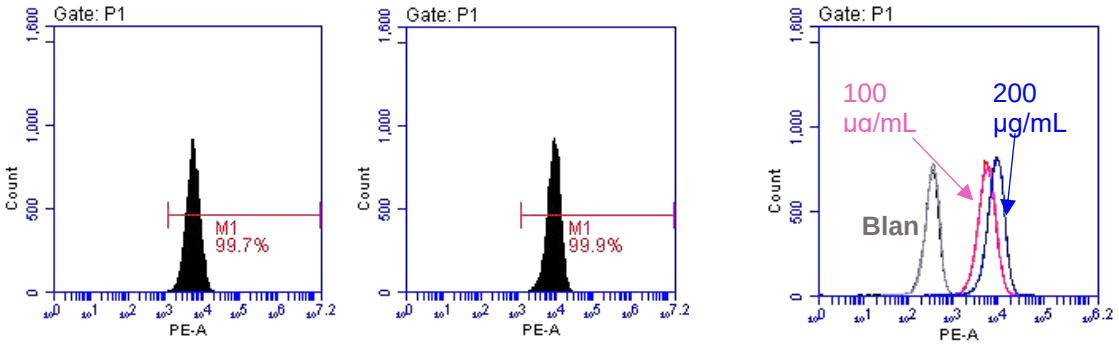

Figure 11 Internalization increased with MION concentration

Adding one more time point of 8-hour incubation, we confirmed that internalization of MIONs increased with time for each type of MIONs (Figure 12). And PolyR group showed constantly better uptake than TAT and PEG only groups.

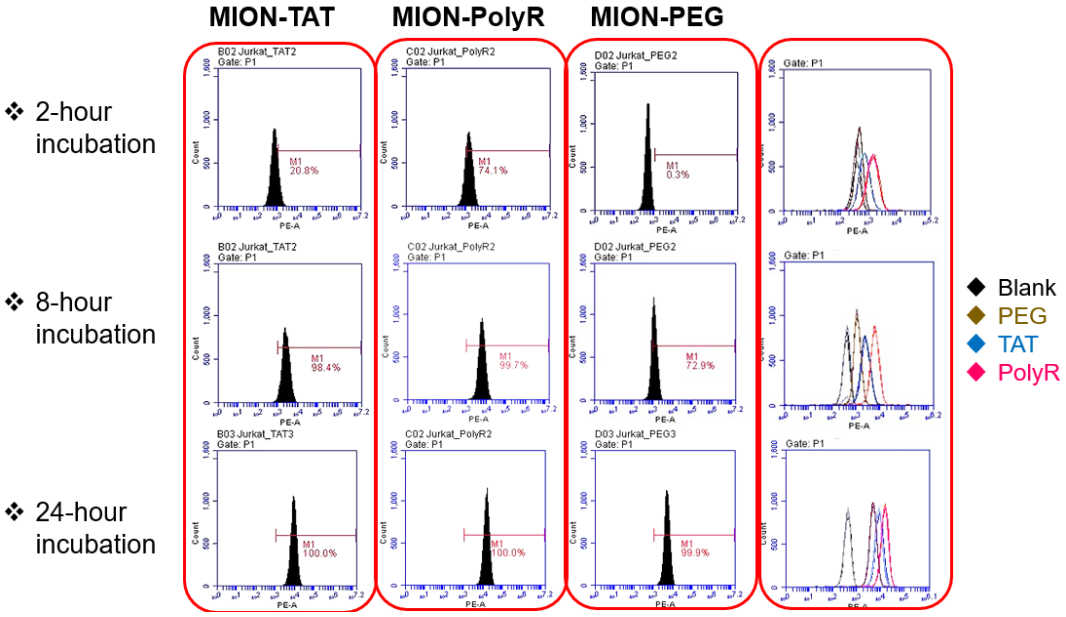

Figure 12 Internalization of MIONs increased with time

Blank control samples collected after 24-hour incubation (GP100 T cells cultured without MIONs) yielded T_2 = 1823.33 ± 136.50 msec, while T_2 relaxivity of MION-PolyR and MION-TAT groups were 912.22 ± 25.89

msec and 1224.44 ± 115.00 msec, respectively. Reduction in T_2 relaxivity signals also confirmed that cellular uptake of MIONs were facilitated by conjugation of both types cell penetrating peptides and prolonged incubation time.

Next, we examined the localization of internalized MIONs. We observed co-localization of MIONs to lysosomes, which was selectively indicated by the white arrows in Figure 13.

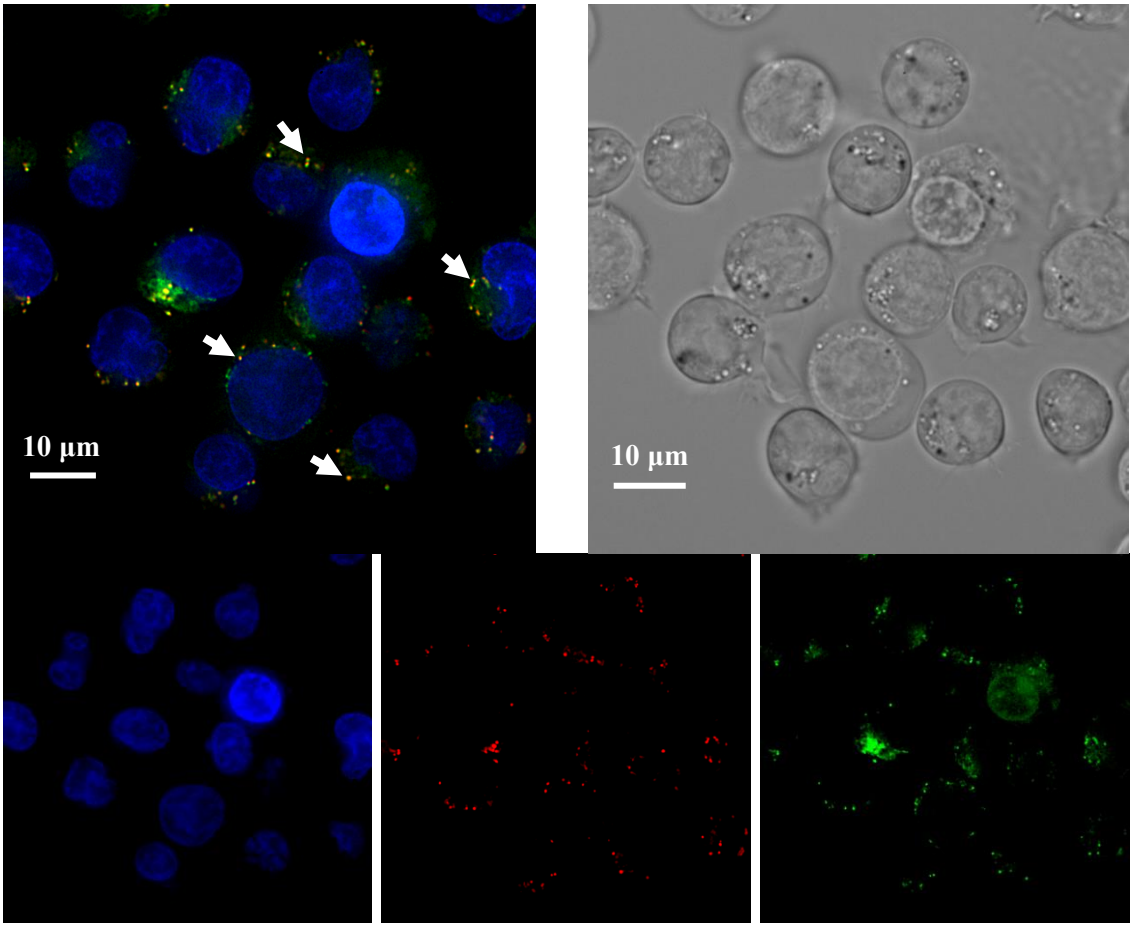

Figure 13 MIONs localized to lysosomes

[Top left: merged figure; top right: bright field; bottom panel (from left to right): the nuclei; the MIONs with DiI; the lysosomes.]

Retention of MIONs in Jurkat cells were observed after 48-hour incubation (Figure 14).

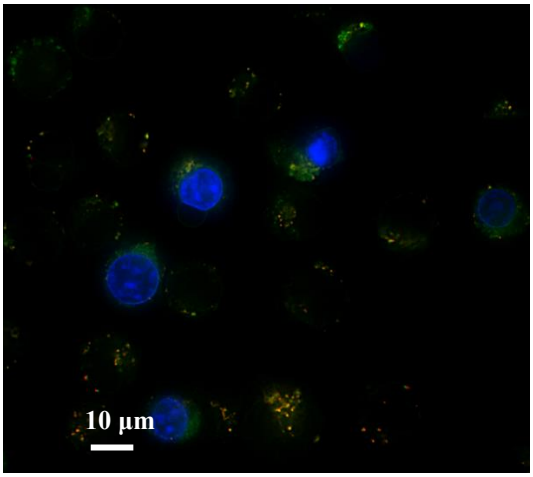

Figure 14 Cells retained PolyR-NPs after 48 hours in culture

When we tried to translate from Jurkat cell line to normal human T cells, we noticed there were some differences in uptake kinetics between these two types of cells. Flow cytometry data after 2-hour incubation demonstrated that naïve T cells internalized much fewer MIONs than Jurkat cells (Figure 15). The fluorescent signals were orders of magnitude lower (Note that the x-axis is of log scale.). We considered that this was partially due to the size differences between T cells and Jurkat cells. A T cell is on average (6~8 µm)[85] half the size of a Jurkat cell (11.5 ± 1.5 µm)[86] in diameter and hence approximately one-eighth the volume of a Jurkat cell.

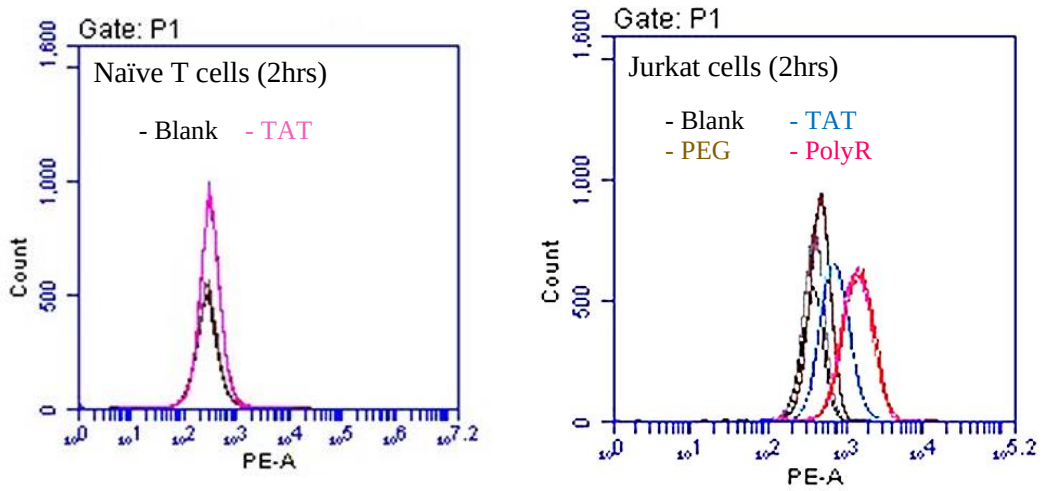

Figure 15 Translation from Jurkat cells to T cells and the difference in uptake kinetics

In addition, after CD3/CD28 activation, T cells changed their morphology from small round spheres to more irregular shapes (Figure 16). They also formed clusters. We hypothesized that these changes could interfere with cellular internalization of nanoparticles and experimental conditions need to be tailored to specific cell types.

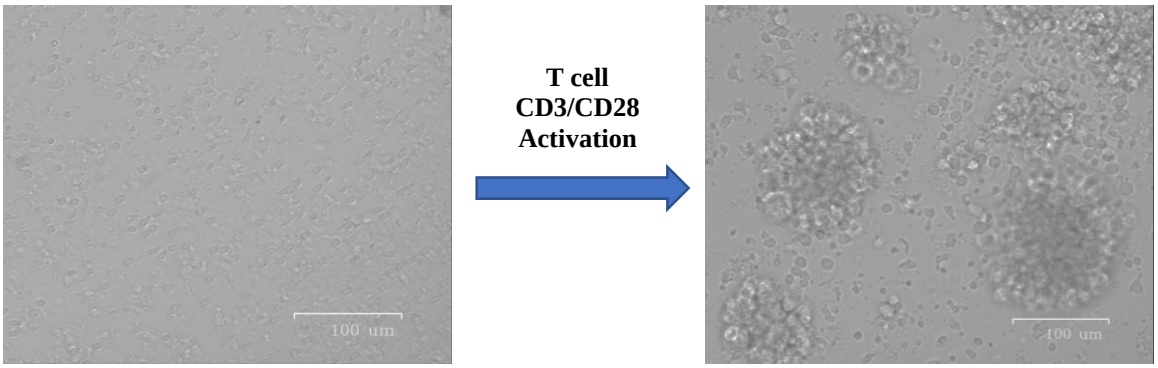

Figure 16 T cell morphological changes before and after activation

After 24-hour incubation, GP100 T cells were able to uptake more MIONs like Jurkat cells (Figure 17). Polyarginine conjugation group also showed better uptake results than the group of TAT conjugation.

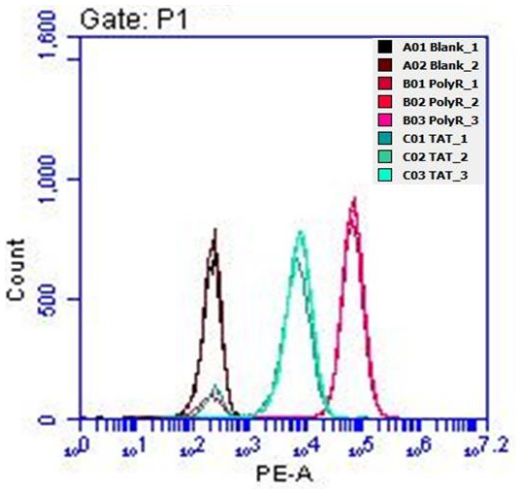

Figure 17 24-hr incubation of GP100 T cells with PolyR-MIONs and TAT-MIONs

Fluorescence signal intensity peaks were displayed as the overlays of each group with triplicate samples. The black/brown peaks to the left indicate cells without MIONs; the turquoise peaks are results of the TAT group; and the red/pinks peaks to the right are the polyarginine group.

2.3 MRI and fluorescence imaging of cells loaded with MIONs

2.3.1 Materials and Methods

Jurkat cells (about 10^7 cells) loaded with MIONs, blank cells and MIONs were mixed 180 µL agarose gel mimicking human body tissue properties and then embedded in six wells of a Ultem® PEI microplate. The 9.4 Tesla Bruker vertical bone MRI scanner at Houston Methodist Translational Imaging Core was used for this phantom study.

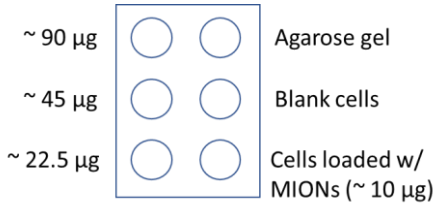

Figure 18 Schematic of microplate layout of MRI phantom study

Cells loaded with MION-TATs and MION-PolyRs were also imaged IVIS imaging platform.

2.3.2 Results and Discussions

We demonstrated that cells loaded with MIONs presented good MRI imaging contrast (Figure 19). Fe content range for MRI phantom imaging of cells loaded with MIONs would need to be further optimized for desirable imaging results to both avoid signal saturation and determine the minimal Fe concentration needed for recognizing cells.

T1_T2map_RARE T1 map T2 map

Figure 19 MRI phantom study of cells loaded with MIONs

Figure 20 demonstrated the possibility of utilizing intravital fluorescence microscopy for tracking the location and migration of cells loaded with MIONs. The blurred spot of image was due to detachment of non-adherent Jurkat cells after removing the magnetic while the chamber

was transferred for imaging. The cell chamber frame displayed autofluorescence of the polymeric materials, but it was of no interference to signals from loaded cells.

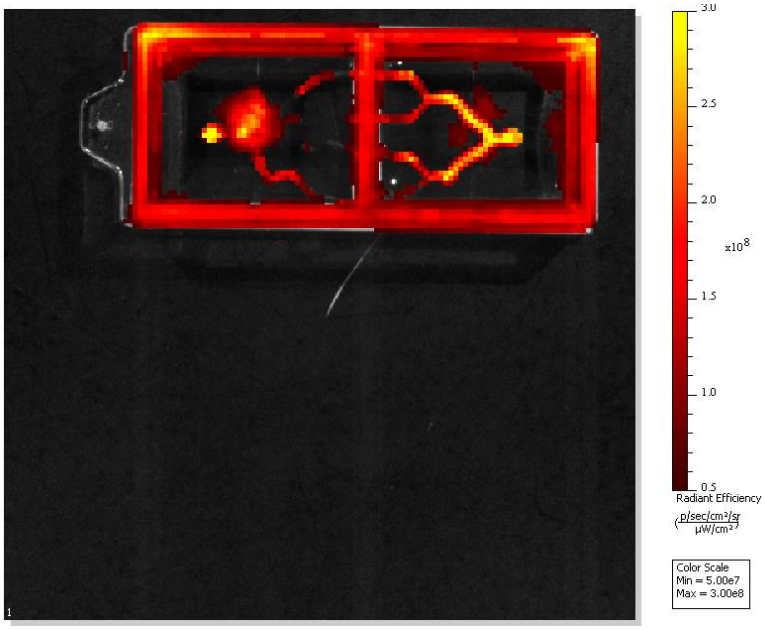

Figure 20 Fluorescent imaging of the magnetically patterned cells

2.4 Magnetic targeting

2.4.1 Materials and Methods

Jurkat cells were seeded at the density of 10^6 cells/mL in a 24-well plate and were incubated for 48 hours with either MION-TAT and MION-PolyR at 200 μg/mL Fe in the incubator. After collecting and washing, 7×10^6 cells from the MION-TAT group and 13.3×10^6 cells from the MION-PolyR group were place into a two-chamber dish. The dish was then placed

on a patterned magnet[55] (Figure 21) and was on shaker at low speed for one hour. We then removed from the magnet before imaging.

Figure 21 Schematic of the pattern of the magnet

2.4.2 Results and Discussions

Figure 22 showed the proof-of-concept result that cells loaded with MIONs could be manipulated by magnetic fields. We observed clear and fast cell migration and accumulation towards the magnet.

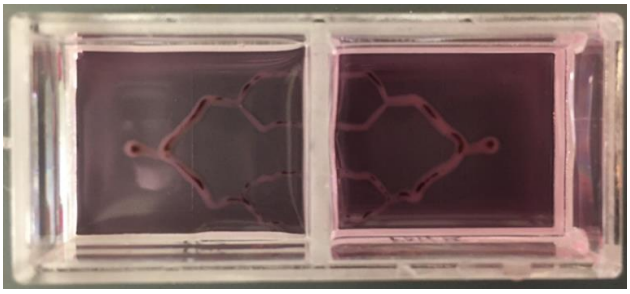

Figure 22 Magnetic patterning and manipulation of MION-loaded Jurkat cells

Figure 23 showed the enlarged view of an area with cell accumulation in line with the pattern of the magnetic underneath previously. Under fluorescence microscopy, we clearly observed increased fluorescence signal intensity from the accumulation of the MION loaded cells compared with the surrounding areas where the magnetic field gradient was not high enough to attract cells.

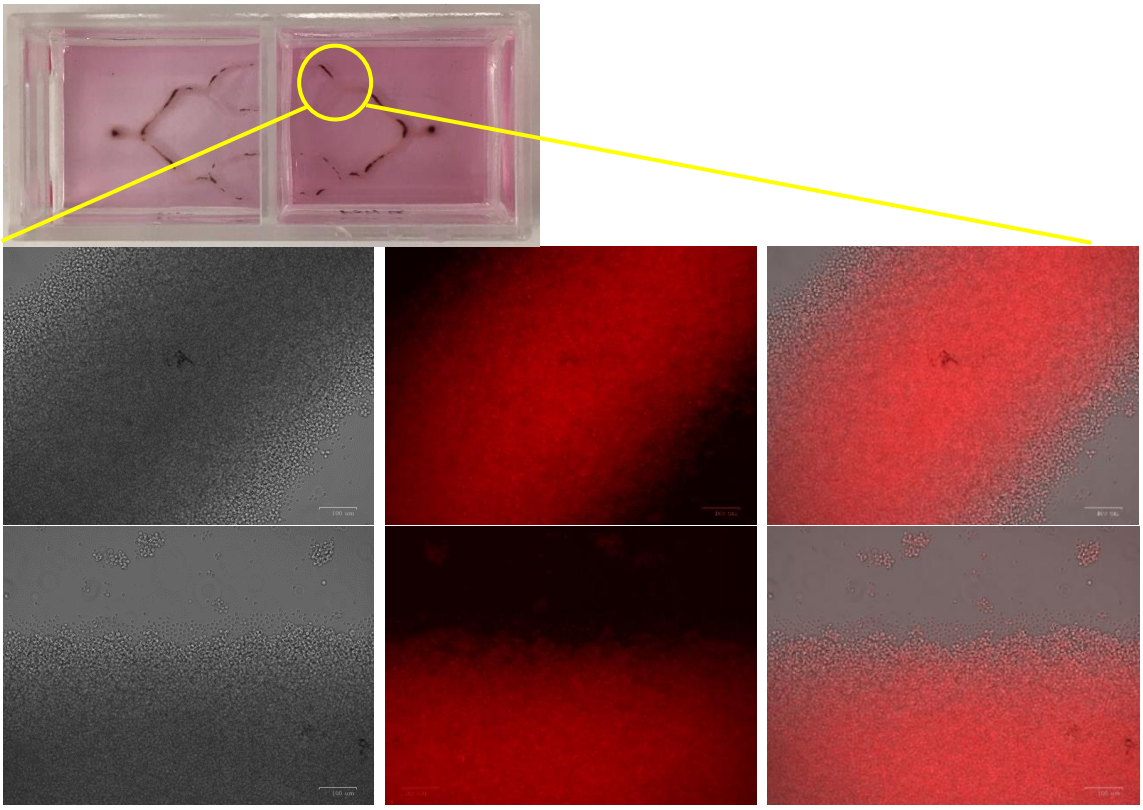

Figure 23 Enlarged view of the magnetic patterned cells under microscope

Left panel: bright field; mid panel: fluorescence signal of DiI; right panel: merged view.

2.5 Conclusions

We demonstrated that MIONs conjugated with both types of cell penetration peptides (polyarginine and TAT) were internalize into cells efficiently without altering cell viability and MIONs with polyarginine (MION-PolyR) gave better delivery efficiency. The successful *ex vivo* labeling of T cells with MIONs as an MRI contrast agent provides the feasibility of tracking T cell *in vivo* using MRI, as well as targeting T cells to tumor sites to enhance therapeutic efficacy for solid tumors.

2.6 Future Work

T cells are agile in the circulation and are non-phagocytic in nature. Therefore, there are fewer endocytosis activities of nanoparticles for T cells compared with phagocytic cell types such as stem cells and macrophages, which are common cell therapy candidates for regenerative medicine and immune modulation. We aimed to generate maximum magnetic force by maximizing the amount of MIONs endocytosed without disturbing normal and therapeutic cellular functions. To further improve the amount of MIONs endocytosed, we could explore other surface modifications of MIONs. For example, chitosan or citric acid coating, and other cell penetrating peptides. We previously also observed slightly lower cell viability in the cells incubated MIONs conjugated with 12-unit poly-arginine compared with those with 9-unit poly-arginine, suggesting the importance of selecting cell penetrating peptides with less detrimental effect on cells. For more accurate intracellular Fe content measurement, inductively coupled plasma mass spectrometry (ICP-MS) could be an alternative to ferrozine assay.

During *in vitro* culture, the disposition of a static external magnetic field under the culture plates may not improve the cellular uptake, because both the gravity and the magnetic force sink MIONs to the bottom of the culture plates and thus reduce the chance of NPs interacting with T cells for

possible endocytosis. In contrast, magnetic levitation[87,88] may help improve the efficiency of endocytosis by maximizing the interactions.

There have been reports about manipulating CAR T cells with MIONs simply associated with the cell membrane, instead of endocytosis[89]. The researchers claimed that they achieved magnetization of cells without interfering cellular functions and magnetic targeting. However, the uncertain detachment of membrane associated MIONs may be a safety concern when translated to *in vivo* studies. Biological assays for evaluating T cell functions after MION loading, sch as T cell proliferation *ex vivo*, migration kinetics under the magnetic field, cytokine release profile in the culture medium, and the tumor killing capacity should also be conducted before moving to *in vivo* studies.

Besides increasing MIONs loading, another aspect to augment the magnetic force is to optimize the shape of magnet and magnetic fields. Some research groups have reported that a U-shape magnet could realize deeper tissue targeting[90]. Dynamically programmable magnetic fields could add another dimension of controlling the movement of cells loaded with MIONs[91]. In addition, it is crucial to simulate and visualize the magnetic field.

There remains an urgent need for the noninvasive *in vivo* tracking of the T cells in patients receiving ACTs to determine their biodistribution, viability, and functionality. Despite the remarkable progress of ACTs in cancer treatment, we still lack the complete understanding of the detailed mechanisms of T cell killing tumor cells[92,93]. Therapeutic progress and results are evaluated largely based on tumor shrinkage and are not monitored real-time. The advances in tracking the transfused cells with emerging molecular imaging technologies and cell-labeling methods could help provide essential information to improve therapeutic efficacy and reduce side effects.

Cellular uptake of MION probes can be readily achieved by simple incubation with minimal cytotoxic effects while ensuring desirable signal intensities; and there is no genetic modification of T cells to reserve their biological functions and not to complicate the safety concerns. However, there are some problems that need to be addressed. First, there is a need to investigate the retention of MIONs by T cells to learn how long the adoptive transfused cells can retain MIONs, and whether they excrete any MIONs. Longitudinal tracking with repetitive imaging requires no signal reduction due to probe excretion or dilution caused by cell division across the whole

therapeutic window. Secondly, the presence of MRI signal due to MIONs is not associated with the viability or functions of the transfused cells.

Design of *in vivo* studies of anti-tumor effect of by locoregional injection of CAR T cells followed by magnetic retention in solid tumors

The ultimate goal of this project is to target T cell to specific anatomical site of solid tumors, especially those that are not easy or even feasible to perform surgical removals. Solid tumors impose many physiological barriers to impede T cell trafficking to the sites[94], such as the dense ECM, the stroma[95], mismatch of cytokine/chemokine receptors and so on. CAR T cells can lose their receptors in circulation and many of them remained in the kidney, the spleen, and the lymph nodes. The percentage of systemically injected T cells finally reaching and accumulating to the tumor sites remains low. Local delivery of T cells has been shown to improve therapeutic efficacy compared with systemically delivered ones, fundamentally eliminating the hurdles for T cell trafficking to tumor sites[96–100]. Other biomaterials-based approaches for *ex vivo* CAR T cell three-dimensional expansion at high cell density, localized delivery of CAR T cells to solid tumors and maintaining CAR T cell persistency and have also been explored, such as injectable thermosensitive hydrogel[101] with

biodegradability for later therapeutic cell egression and thermally reversible shape memory thin films[102]. We reasoned that the anti-tumor effect of locoregional injected CAR T cells can be further enhanced by magnetic retention within solid tumors.

The selection of mouse tumor model for could be human xenograft model generated by subcutaneous inoculation of cancer cell line. Orthotopic tumor model would also be very valuable in demonstrating the therapeutic efficacy of our magnetic targeting approach and for translation from murine models to human clinical trials.

To validate our hypothesis, we designed the *in vivo* study with three key sections (Figure 24; adopted from Ref [99]):

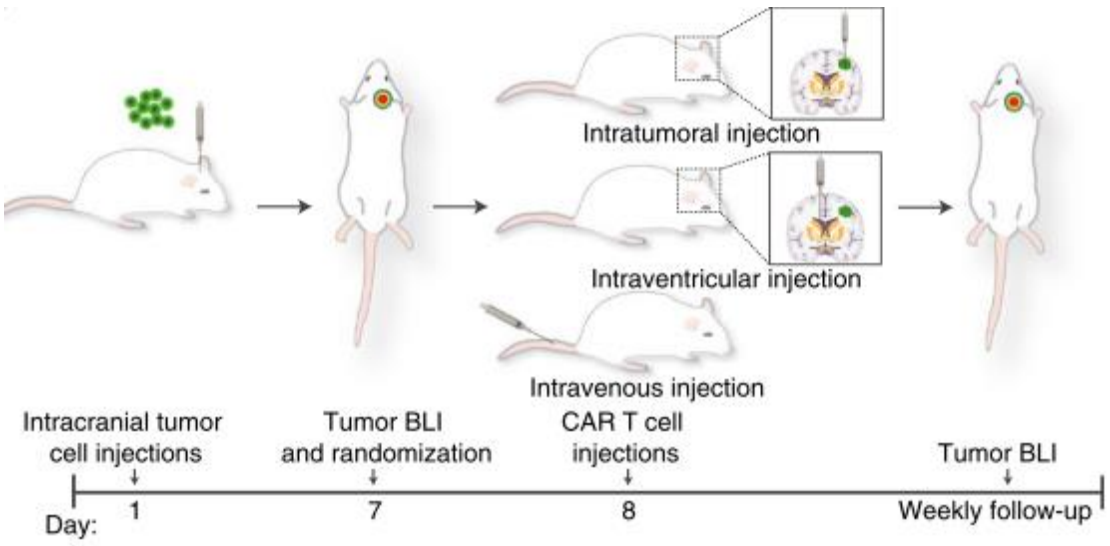

Figure 24 Experimental overview of the evaluation of *in vivo* efficacy of CAR T cells comparing different routes of administration

First, we would want to compare the therapeutic efficacy of CAR T cells administrations by different routes both with and without the magnet field, including local/intratumoral injection (5 million cells in 5 μL total volume), regional/intraventricular injection, and systemic/intravenous (IV) (5 million cells in 50 μL total volume into the dorsal tail vein). The time window and location of magnet placement would be optimized meanwhile.

Secondly, we would want to compare if longer-term retention of a single dose injection could avoid T cell exhaustion in solid tumors and outperform repeated injections during tumor elimination. Optimization of CAR T cell dosages would be favorable to reduce side effects.

Finally, we would want to investigate whether CAR T cells retained by magnets during tumor eradication can also be effective in treating metastasize or secondary tumors, eliciting abscopal effect and systemic immune response to tumors, and whether protection also differs according to the routes of administration. We could re-challenge cured mice in the contralateral cerebral hemisphere with the same tumor line 40 days after infusion of one dose of IT, ICV or IV CAR T cells. To evaluate if CAR T cells delivered ICV and/or IV provide protection from re-challenge with peripheral tumors, we could re-challenge mice with antigen-specific gene knockout or parental cells in the flank. Immunohistology of T cell

subpopulations and statuses in solid tumor tissues would reveal vital information about therapeutic efficacy of each treatment conditions.

It would also be valuable to evaluate the synergistic effect of administering multiple subsets of CAR T cells with different targeting molecules. This could also be further advanced to targeting more personalized neoantigens if combined with bioinformatics technologies for screening neoantigens. Injecting different or mixed compositions of various functional T cell subpopulations[103] and the optimal sequence of administration would be worth exploration as well, where the endocytosed MIONs may also serve the purpose of magnetic separation.

Nevertheless, regional/local/intratumoral injection is not the solution to everything. Local instillation is often more technically challenging and can be more invasive than simple systemic/intravenous administration. The elevated interstitial fluid pressure and mechanical stress within the solid tumor could limit the volume of therapeutic cell injection. The ability of these locoregionally delivered CAR T cells to exit the tumor and then traffic to other tumor sites (such as the numerous metastasized secondary tumor sites in advanced cancer patients that are not clearly defined) is uncertain.

However, there are many cases of solid tumors that are not easily accessible or even inoperable, where systemic injections of therapeutic cells may be the only administration route available. For example, tumors in a sensitive location such as the spinal cord, brain cancer that surgically extract of the surrounding tissue will harm the patients, tumors in bone marrow, metastatic tumors that are hard to remove safely, and the situation where the patient has other medical conditions that limit the ability to withstand surgery. To this end, we hypothesized that local retention of MION-loaded therapeutic cells by placing an external magnetic field over the identified regions of tumors could be beneficial to improving therapeutic efficacy. For in vitro studies, the magnetic capture and retention of loaded cells can be demonstrated by using microfluidic devices to mimic the circulation at different physiologically relevant capillary blood flow velocities (such as 5 mms^{-1} (0.037 mL/min), 8 mms^{-1} (0.060 mL/min) and 10 mms^{-1} (0.075 mL/ min)) with a magnet placed on the side or bottom of the microfluidic channels and at different distances from them (e.g. 0, 3, 6, 8, 11 and 14 mm).

The immunosuppressive tumor microenvironment significantly hampers the killing capability of CAR T cells delivered[104]. Ameliorating the immunosuppressive condition and even reprogramming the harsh tumor microenvironment into a more supportive environment for therapeutic cells

represents a radical and promising strategy to pave the way for cancer immunotherapies using CAR T cells[105–107]. Several strategies have been developed to perturb and prime the tumor microenvironment[108], induce immunogenic cell death (ICD) and abscopal killing effect, and re-direct regulatory cell populations for synergistic effects. It would be beneficial to identify better combinational therapies with other therapeutic approaches[109], such as the use of checkpoint inhibitor blockade and bispecific antibodies[110] to engage and boost T cells.

Chapter 3: To improve heating efficiency of MIONs by mesoporous silica coating for hyperthermia and heat-triggered release and delivery of anticancer drug

3.1 Introduction

Mesoporous silica structure has garnered considerable attention from biomedical engineers due to their ordered pore network, high surface area, large pore volume and the possibilities for further functionalization[111]. These advantages can be utilized for drug and biomolecule delivery purposes of large loading capability[112] and protection of the molecules[113]. Synthesis methods and property characterizations of mesoporous silica coating on MIONs has been extensively explored for different biomedical applications[114–120].

As introduced in Section 1.2.3, MIONs can convert electromagnetic energy into thermal energy by relaxation under an alternating magnetic field (AMF). The incorporation of MION core endues the nanostructure the capability of heat triggered drug release to realize spatial-temporal control upon activation of the alternating magnetic field. However, aggregation of MIONs in aqueous environments limits their heating efficiency[4]. To address this issue, we optimized MIONs with a uniform layer of mesoporous silica

coating to improve their colloidal stability and hence heating efficiency. This MION formulation can be employed for cancer hyperthermia treatment and heat-triggered anticancer drug delivery.

3.2 Experimental Design

Surfactant templated sol-gel method was adopted to synthesize the core-shell structured magnetic iron oxide nanoparticles with mesoporous silica coating[118] (Figure 25). Hexadecyl trimethyl ammonium bromide (HTAB) serves both as a surfactant (or phase transfer agent) and an organic template for growing mesoporous silica layer on MIONs. The alkyl chains of HTAB interdigitate to the oleic acid chains of MIONs through the hydrophobic van der Waals interactions. The hydrophilic head groups of HTAB facilitate the aqueous dispersion of MIONs with thermodynamically defined bilayer structures. The synthesized particles were characterized by various modalities for their physical-chemical properties.

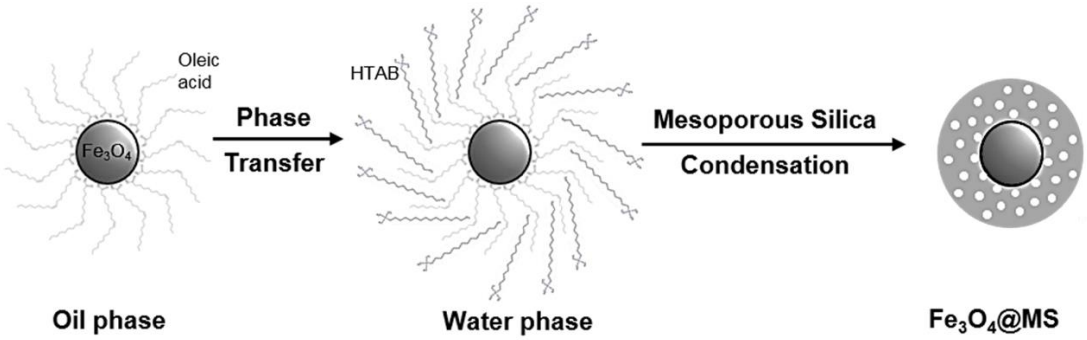

Figure 25 Mechanism of mesoporous silica coating onto oleic acid capped MIONs

3.3 Materials and Methods

Magnetic iron oxide nanoparticles were synthesized by thermal decomposition of iron acetylacetonate using an established protocol and by stepwise seed-mediated growth to reach an average diameter of 20nm confirmed by TEM imaging[4]. The as-synthesized MIONs were transferred from toluene to chloroform for mesoporous silica coating. 20nm MIONs of this same batch were also coated with PEG2K using the dual solvent exchange methods[5]. We used hexadecyltrimethylammonium bromide (HTAB) (H5882 SIGMA, >98% purity) as the surfactant and the template for tetraethyl orthosilicate (TEOS) (131903 ALDRICH, 98% purity) adsorption. The pH of the reaction was adjusted to 10.5-12 by adding 8M NaOH. Details of the synthesis protocol can be found in ***Appendix***.

The size and size distribution of pure iron oxide nanoparticles and mesoporous silica-coated nanoparticles were measured using transmitted electron microscopy (TEM) (JEOL 2100F) and dynamic light scattering (DLS) (Wyatt Möbiuζ®). The Ted Pella TEM Carbon Type-B grids were glow-discharged to hold hydrophilic mesoporous coated MIONs. Magnetic susceptibility of the nanoparticles was measured with a Quantum Design MPMS SQUID magnetometer. The X-ray diffraction (XRD) analysis was

conducted to investigate the nanoparticle crystal structure (Rigaku SmartLab).

Magnetic fluid heating in solution was conducted using an Ameritherm EASYHEAT Induction Heating System for 120 seconds (324kHZ, 150A). 1 mL 1mg/mL Fe of the sample was prepared for triplicate SAR measurements. Pure water and PEG2K coated MIONs of the same Fe concentration served as the controls for SAR measurements.

3.4 Results and Discussions

Before coating, MIONs and pure mesoporous silica particles were characterized by TEM (Figure 26).

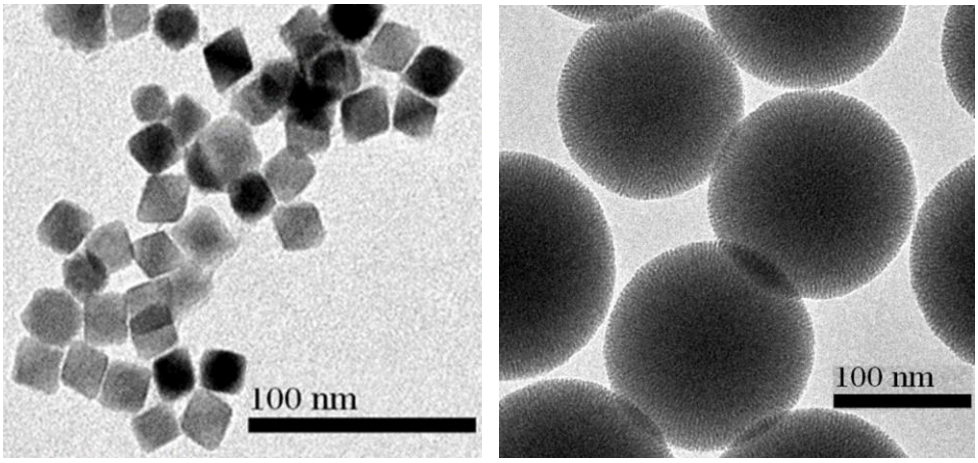

Figure 26 TEM images of pure MIONs (left) and pure mesoporous silica particles (right)

TEM image (Figure 27) confirmed that there was an even layer of mesoporous silica coating on each MION, with the MION core in the center and a homogeneous silica shell of about 20nm in thickness. Mesoporous

structure can be clearly observed. The size distribution of the coated particles was 61.43 ± 0.09 nm measured by DLS (polydispersity: 4.47 ± 0.46 nm). Mesoporous silica coated MIONs remained stable and homogeneous in water over a week as indicated by only slightly increased value in polydispersity measured by DLS.

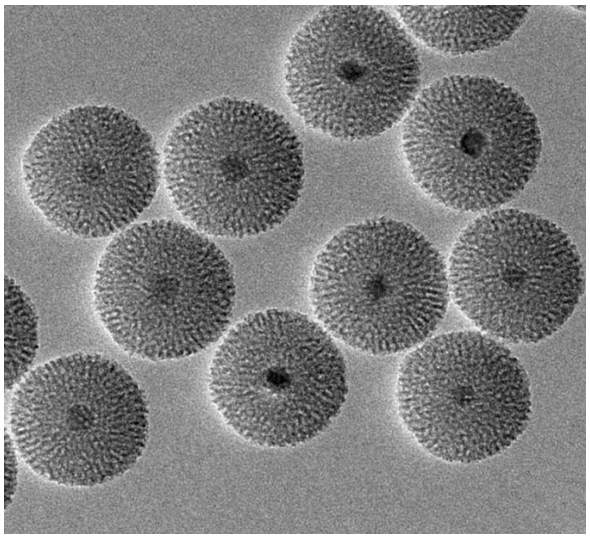

Figure 27 Representative TEM images of mesoporous silica coated MIONs

XRD pattern (Figure 28) showed a broad peak near 2θ = 20°, indicating the existence of mesoporous silica. Peaks at higher angles can be indexed to Fe_3O_4, in agreement with the XRD pattern of pure MIONs.

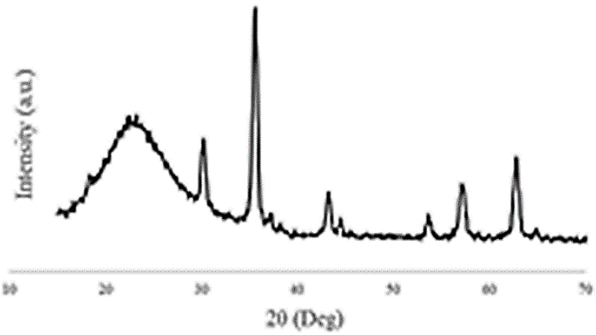

Figure 28 XRD pattern of mesoporous coated MIONs

Room temperature magnetization curve of the coated iron oxide nanoparticles measured by SQUID (Figure 29) showed a similar hysteresis pattern to uncoated MIONs, indicating the mesoporous coating did not influence the saturation magnetism of MIONs.

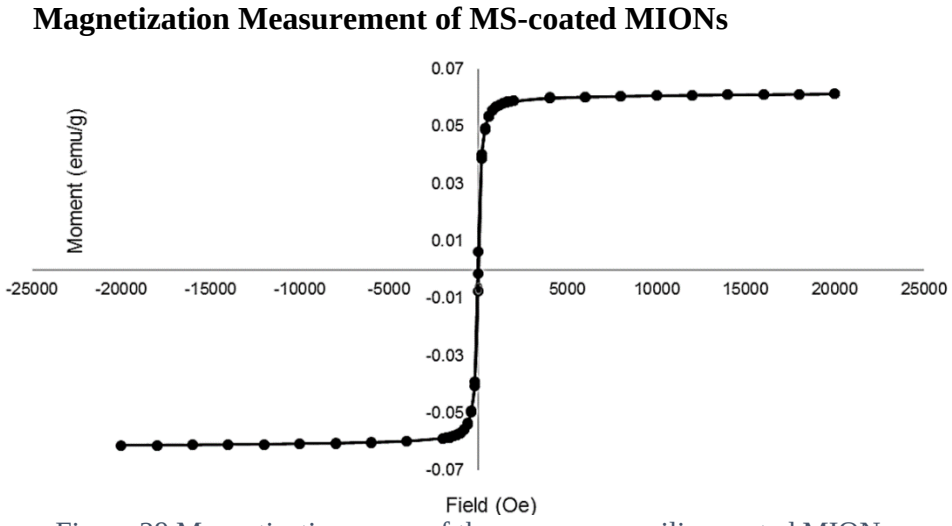

Figure 29 Magnetization curve of the mesoporous silica coated MIONs

The temperature of the ferrofluid was measured as a function of time, and the slopes of the heating profiles were used to calculate the SAR values of each type of nanoparticles (Equation 3). Heating profiles in water under the alternating magnetic field (Figure 30) revealed improved heating efficiency of the mesoporous silica-coated nanoparticles compared to PEG2K-coated MIONs. The SAR value of mesoporous silica coated MIONs was calculated to be 337.8 ± 3.3 W/g Fe and the SAR value of PEG2K-coated MIONs was 244.0 ± 1.8 W/g Fe (N=3). This was mainly contributed

by enhanced colloidal stability and hence reduced aggregation of nanoparticles.

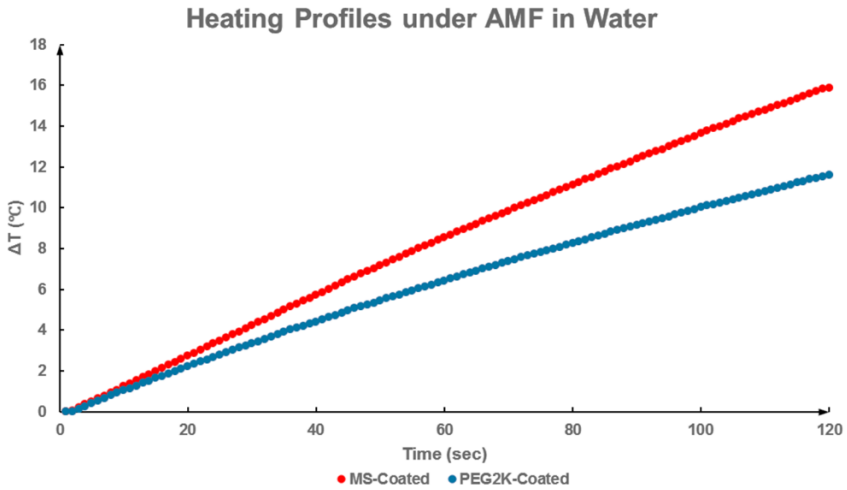

Figure 30 Heating profiles of mesoporous silica-coated and PEG2K-coated MIONs in water

3.5 Conclusion

Colloidal stability of the previously hydrophobic MIONs in aqueous environments, such as water and ethanol, were greatly improved by mesoporous silica coating. Mesoporous silica coating on magnetic iron oxide nanoparticles well preserved their excellent magnetic properties and improved magnetic heating efficiency by preventing aggregation.

3.6 Future work

As previous findings suggested, the heat efficiency of MIONs increased significantly with the size of the nanoparticles[4]. With a modified

dynamic hysteresis model, the SAR value of 40nm MIONs approached the theoretical limit[4]. Utilizing larger MIONs with enhanced colloidal stability and heating efficiency may be especially advantageous for the application of hyperthermia for solid tumor treatment. The larger the nanoparticles, the more need of maintaining colloidal stability to counteract the inter-particle magnetic interactions to avoid aggregation. Therefore, successful mesoporous silica coating on MIONs of larger sizes is desirable. Besides the 20nm MIONs, we also tried to coat 30nm MIONs with mesoporous silica. However, the yield was very low due to initial poor dispersity of MIONs. There was a myriad of small empty silica particles without a MION core and purification steps would remove aggregated MIONs without successful coating, resulting in very low yield of coated MIONs (Figure 31). Thus, it warrants further systematic optimizations of adjusting coating thickness to various applications by changing the amount of TEOS, and the ratios between each reagent.

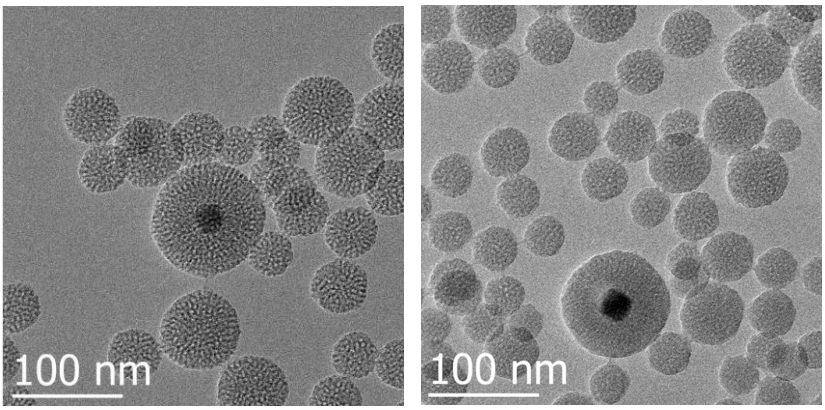

Figure 31 Representative TEM images of mesoporous silica coating on 30nm MIONs

For drug delivery applications, potential drug candidates include Doxorubicin[121], free-radical generating agents such as AAPH[122] to modulate the solid tumor microenvironment and so on. Drugs can be loaded onto the magnetic nanoparticles via hydrophobic interaction or electrostatic interaction depending on the surface characteristics. Upon systemic administration, nanoparticles can interact with serum proteins in circulation resulting in the formation of "protein corona" on the surface[123,124]. It is crucial to investigate the relationship between nanoparticles' "chemical identity" and "biological identity" to improve their clinical translations. Further surface modification methods, such as polymer and bovine serum albumin (BSA) coating, can be adopted to enhance biocompatibility and stability in more biological relevant settings. Mesoporous silica coating can also enhance MRI signal intensity because the permeability of mesoporous coating to H_2O decreases longitudinal relaxivity, which can be beneficial for potential imaging applications[115,116,125].

Nanowarming is another potential application of mesoporous silica coated MIONs for tissue and/or organ transplantation[126]. Conventional re-warming processes of the previously cryopreserved tissue/organs induce thermal-mechanical stress due to non-homogeneous and slow heating process. Magnetic nanoparticles with excellent colloidal stability in

cryoprotectant agents (CPA) can uniformly diffuse through the vasculatures of the organs and generate more uniform heat under the alternating magnetic field. Improvement on heating efficiency in tissue volumes larger than 50ml is a critical need. Scaling-up and control over batch variance are also important issues to address for nanoparticle applications[127]. Although it is beyond the scope of this study, it is worth further development.

Chapter 4: To measure the levels of trace biomarkers for early cancer detection with high sensitivity

4.1 Introduction

Pancreatic cancer is the 4th lethal cancer type in the United States[128]. It is estimated that over 56,000 new cases are diagnosed each year and over 45,000 people die because of this cancer annually[128]. The pancreas locates deep in the body and patients at early stages are usually asymptomatic. Because of this, pancreatic cancer is extremely hard to be diagnosed early. Most patients with pancreatic cancers are diagnosed at an advanced stage where cancer cells have already metastasized to other organs and when treatment options are limited. Therefore, it is beneficial to develop methods for early diagnosis of pancreatic cancers to improve treatment outcomes.

As an auxiliary method to imaging and biopsy tests, blood sample tests can be used to check the levels of biomarkers for pancreatic cancer diagnosis. Elevated levels of these markers shed by pancreatic cancer cells, such as CA19-9 (>37 U/mL), CA125 (>46 U/mL) and CEA (>3 ng/mL), may indicate the presence of pancreatic cancer[129–131]. In addition, levels of these biomarkers can be used to monitor treatment processes.

We have developed iron oxide nanoparticle linked immunosorbent assay (ILISA) technology[72,73] for biomarker detection with high sensitivity. The advantages of ILISA over conventional ELISA also lie in the good linearity, large dynamic range, and more importantly reproducibility (Figure 32-34).

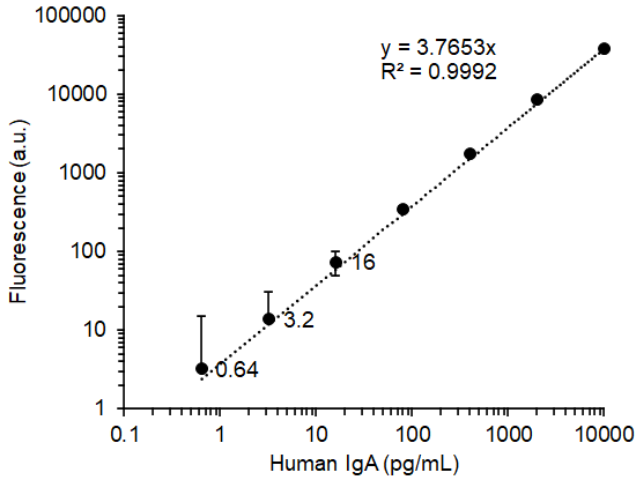

Figure 32 ILISA showed sensitivity and good linearity

Purified human IgA was used as an example; detection limit: 0.64 pg/mL (= 2.1 pM) (data courtesy of Dr. Linlin Zhang).

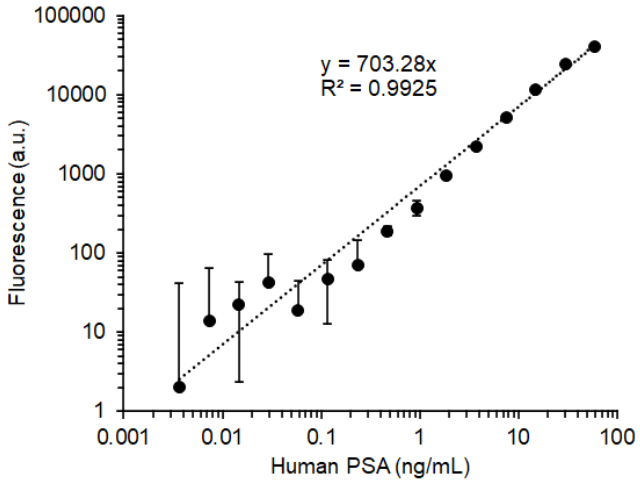

Figure 33 ILISA showed large dynamic range

Purified human IgA was used as an example; assay range: 30-0.0037 ng/mL (data courtesy of Dr. Linlin Zhang).

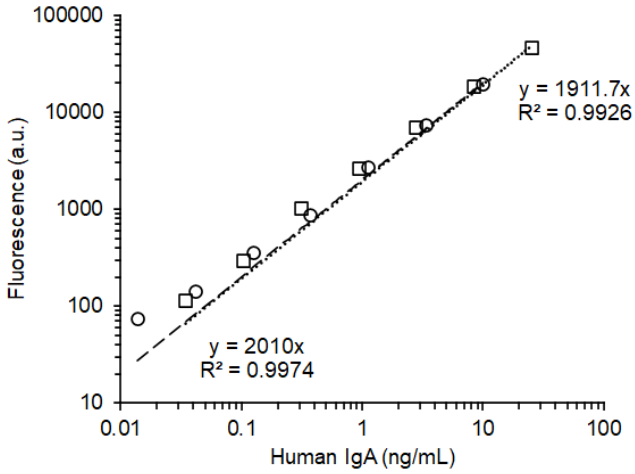

Figure 34 ILISA showed great reproducibility for multiple test rounds

Purified human IgA was used as an example; (data courtesy of Dr. Linlin Zhang).

To further amplify the signal intensity and hence detection limit, we doped europium (Eu)[132] (Figure 35), a rare earth element, into the MIONs for using time-resolved fluorescence (TRF). TRF was first introduced in 1980s in pursuit of reducing background signal (e.g. autofluorescence from biological samples) and enhancing detection sensitivity of the fluoroimmunoasssays[133,134]. The background fluorescence usually has a faster decay time compared with fluorescence intensity offered by a lanthanide, e.g. Eu^{3+}, or a lanthanide chelator. Therefore, the temporal separation of the long-lived emission measured after a selected delay time almost completely eliminates the undesirable background signal, achieving higher specific activity[135] (Figure 36).

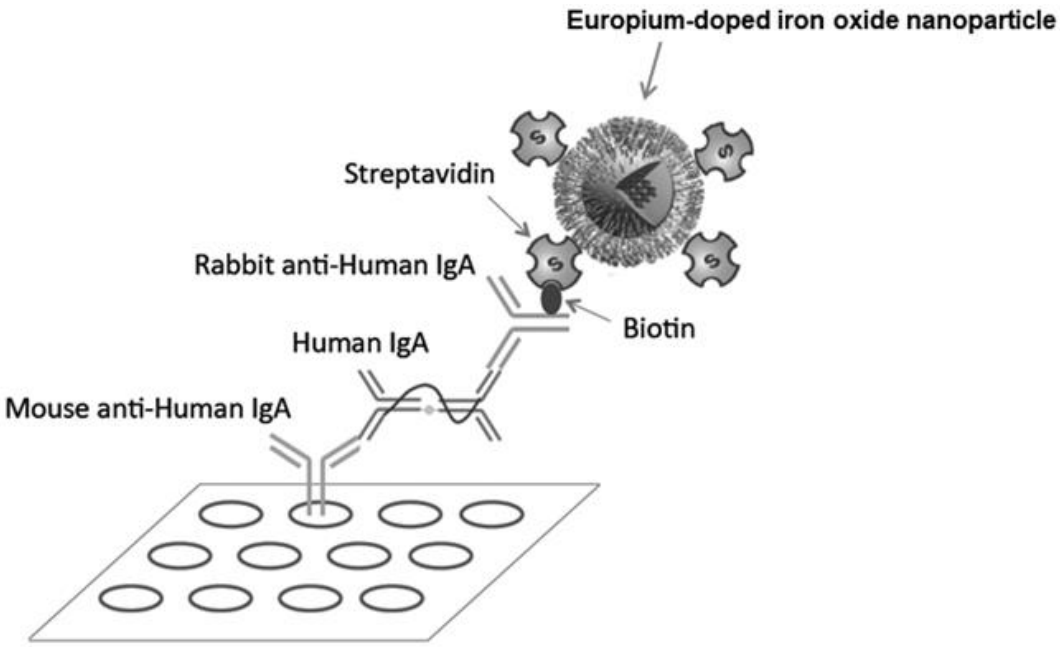

Figure 35 Illustration of ILISA using Eu-doped MIONs and human IgA as an example

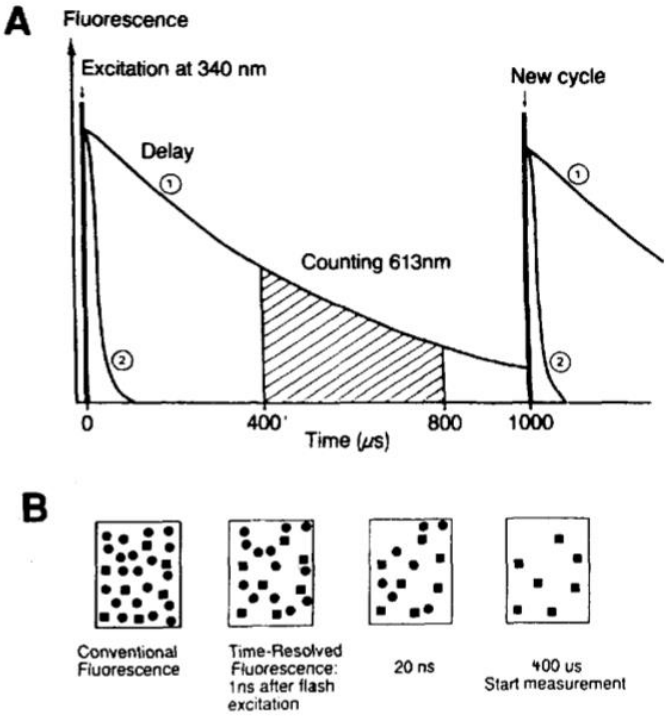

Figure 36 Principle of time-resolved fluorometric measurement

(A) Exponential decay of short-lived ② and long-lived ① fluorescence. The latter is quantified in a selected time-window as shown. (B) Events occurring in the cuvette during the time-resolved fluorometric measurement at various time periods. Long-lived and short-lived fluorescence is represented by squares and circles, respectively[136].

4.2 ILISA for pancreatic cancer biomarker detection using patient serum samples

4.2.1 Experimental Design

We first tested our optimized nanoparticle probes with commercially available ELISA kits for CA19-9, CA125 and CEA, and focused on CA19-9 measurement. We then validated our ILISA platform by measurement of mock samples. Mock pancreatic cancer patient serum samples were created by adding human CA19-9 to pooled healthy human serum at designated concentration. The samples were analyzed with a sandwich immunosorbent assay and the streptavidin- Eu_xFe_yO probe. Finally, we measured the CA19-9 levels in patient serum samples.

4.2.2 Materials and Methods

Europium-doped iron oxide nanoparticle (Eu_xFe_yO NPs) were synthesized based on our established protocol for synthesizing pure MIONs[4] and modified by replacing 15% of $Fe(acac)_3$ with $Eu(acac)_3$. Eu_xFe_yO NPs were characterized for size by TEM and europium doping ratio by calculation based on Eu standard curve. Modification of streptavidin for conjugation with Eu_xFe_yO NPs was adopted and modified from Ref[137]

(Figure 37). DELFIA® Enhancement Solution was used for europium fluorescence.

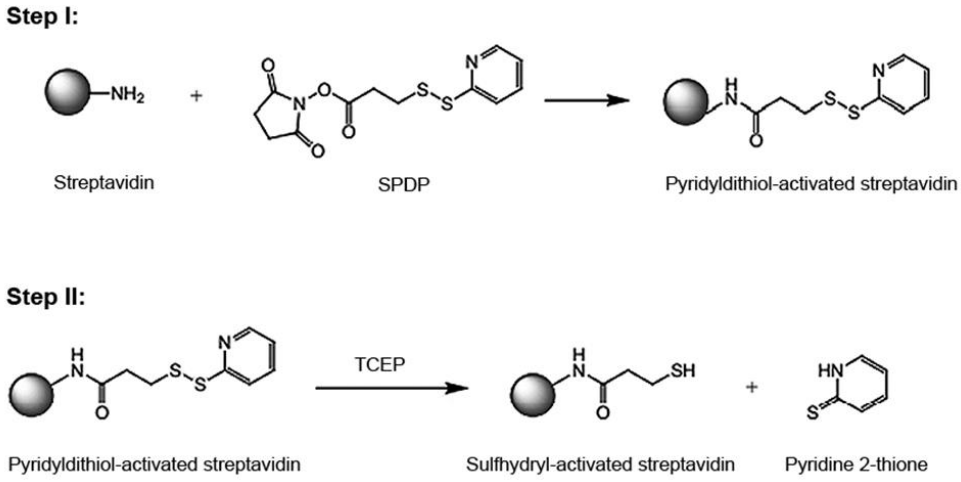

Figure 37 Schematics of modification of Eu_xFe_yO with streptavidin

The commercially available ELISA kits for CA19-9, CA125 and CEA were RayBio® Human CA19-9 ELISA Kit, RayBio® Human CA125 ELISA Kit, and Human CEACAM-5/CD66e DuoSet ELISA, respectively.

There were two batches of cryopreserved patient serum samples were gifts from MD Anderson Cancer Center. We selected a total of 24 patient serum samples for measurement (N = 24), nine females and 15 males (detailed information listed in *Appendix-II*). We re-label the IDs of the samples for easy recording of results. The selection criteria were as the followings: with “Location in Pancreas” as “Head”; age no younger than 50

years old. The ethnic components were 21 white, one black or African American, and two others.

Patient serum samples were thawed to room temperature before use. 90μL of patient serum were diluted five times using Assay Diluent C (Item L) from RayBio® Human CA19-9 ELISA Kit (Catalog #: ELH-CA19-9). 100μL of diluted serum was added into each well of CA19-9 microplate coated with anti-human CA19-9 and measured with a sandwich immunosorbent assay and the streptavidin-EuFeO probe. The pooled serum from healthy persons was used as the control. Each sample was measured in triplicates. TRF readout was done by TECAN SPARK plate reader.

4.2.3 Results and Discussions

4.2.3.1 Characterizations of Eu-doped MIONs

The size of the europium-doped iron oxide nanoparticles was 8.5 ± 1.0 nm measured by TEM (Figure 38). Doping rate of europium was measured by fluorescence plate reader and calculated based on Eu standard curve to be 5.2%, corresponding to 674 Eu atom per particle and that the molar ratio of Fe/Eu was 18.2 (data courtesy of Dr. Sheng Tong and Dr. Linlin Zhang)..

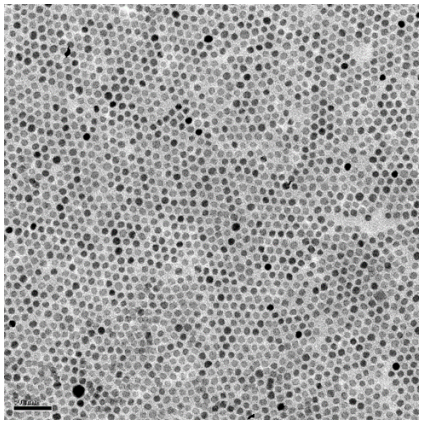

Figure 38 TEM image of Eu-doped iron oxide nanoparticles

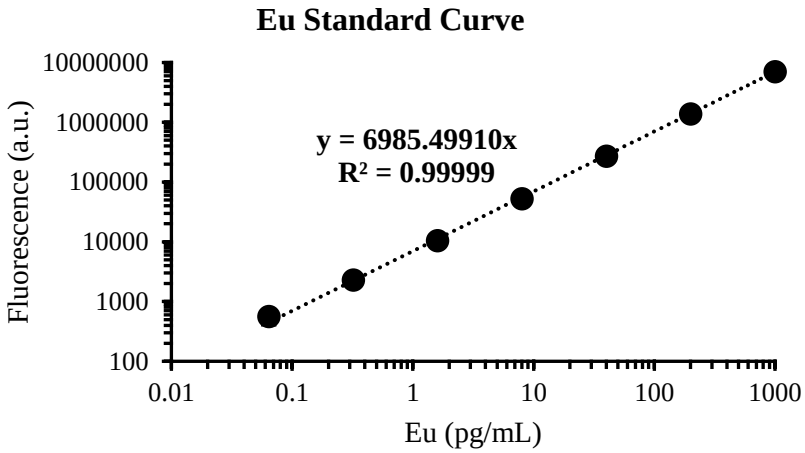

Figure 39 Standard curve of europium

4.2.3.2 Pancreatic cancer biomarker measurements using antigens from commercially available ELISA kits and ILISA platform

We first tested Eu_xFe_yO NP probes with commercially available ELISA kits for CA125. Standard curve of CA125 with respect to concentration-fluorescence signal was generated (Figure 40 and Tale 3). Based on the regression equation obtained, we calculated that the absorbance value of CA125 level in normal serum samples (<46 U/mL) should be less than 0.268.

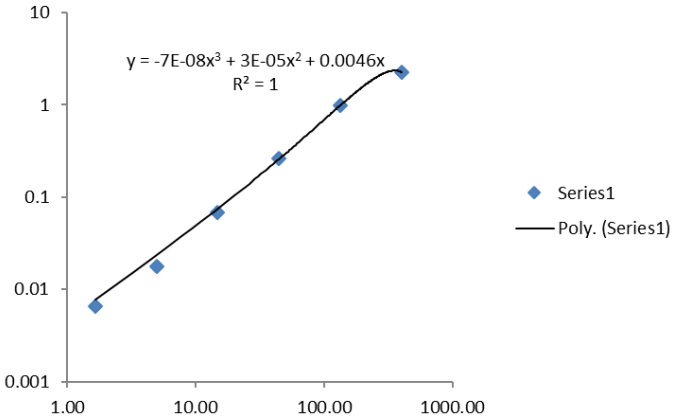

Figure 40 Standard curve of CA125 measurement

U/mL	STD_1	STD_2
400	2.322	2.313
133.3333	1.017	1.063
44.44444	0.318	0.321
14.81481	0.126	0.127
4.938272	0.077	0.074
1.646091	0.063	0.066
0.548697	0.057	0.068

Normal Range
< 46 U/mL (< 0.268 absorbance readout based on standard curve)

Table 3 Fluorescence signal value corresponding to CA125 concentration

However, we observed that for all ten patient serum samples we measured (Table 4, left panel), the signal intensities were all lower that 0.268, which means that the CA125 levels were lower than the normal CA125 range.

0.066			
0.11			
0.211			
0.05			
0.043	RiceBao_3	0.087	10X
0.065		0.13	5X
0.056	RiceBao_2	0.111	10X
0.048		0.117	5X
0.1	RiceBao_1	0.057	10X
0.069		0.054	5X

Table 4 Absorbance signal readouts of CA125 levels in ten patient serum samples

Left column corresponded to Sample 1-10 and the right two columns corresponded to the first three samples with 5X and 10X dilutions.

Similarly, we tested Eu_xFe_yO NP probes with commercially available ELISA kits for CEA. Standard curve of CEA with respect to concentration-fluorescence signal was generated (Figure 41 and Table 5).

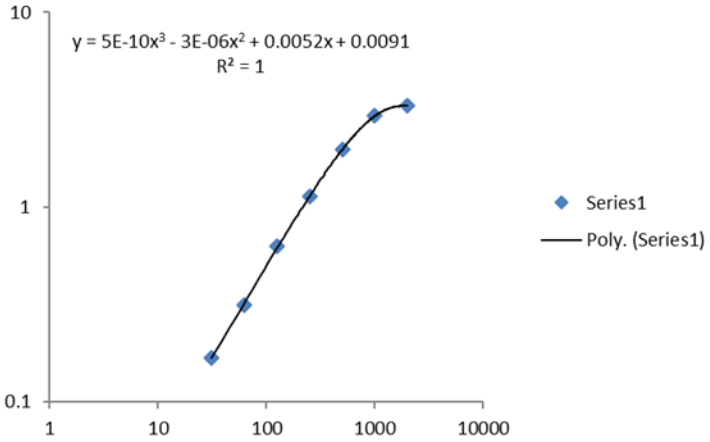

Figure 41 Standard curve of CEA measurement

pg/mL	STD_1	STD_2
2000	3.912	4.036
1000	3.478	3.684
500	2.481	2.759
250	1.727	1.825
125	1.23	1.317
62.5	0.96	0.963
31.25	0.794	0.834
0	0.641	0.652

Table 5 Fluorescence signal value corresponding to CEA concentration

0.134			
0.096			
0.102	0.102	5X	S_1
0.083	0.092	10X	
0.083	0.084	5X	S_2
0.104	0.095	10X	
0.088	0.073	5X	S_4
0.086	0.047	(N/A)	
0.096			
0.11			

Table 6 Absorbance signal readouts of CEA levels in ten patient serum samples

Left column corresponded to Sample 1-10 and the right column corresponded to Samples #1, 2 and 4 with 5X and 10X dilutions.

However, we observed that all ten patient sample absorbance readouts were lower than background signal as highlighted in Table 5.

The reasons why commercial ELISA kit integrated with our Eu_xFe_yO NP probes failed to quantify CEA and CA125 could be multiple. A meta-analysis has shown low sensitivity of CEA in diagnosing pancreatic cancer due to intrinsic biological characteristics[138]. There might also be artifact in sample preparations or incompatibility of Eu_xFe_yO NP probes with the commercial kits.

Finally, we tested Eu_xFe_yO NP probes with commercially available ELISA kits for CA19-9. Standard curve of CA19-9 with respect to concentration-fluorescence signal was generated (Figure 42 and Table 7).

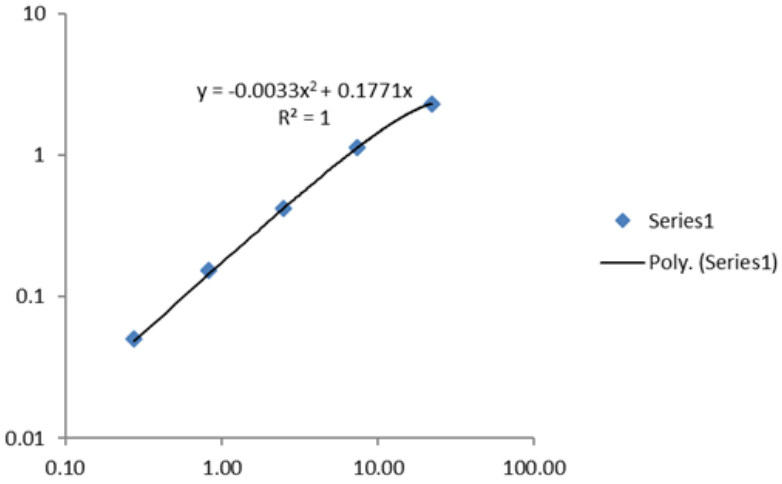

Figure 42 Standard curve of CA19-9 measurement

U/mL	STD_1	STD_2
200.000	3.898	OVRFLW
66.667	3.517	4.029
22.222	2.264	2.486
7.407	1.169	1.202
2.469	0.473	0.493
0.823	0.206	0.217
0.274	0.108	0.109
0.000	0.06	0.057

Normal Range
0~37 U/mL (< 2.035 absorbance readout based on standard curve)

Table 7 Fluorescence signal value corresponding to CA19-9 concentrations

For patient sample measurements (Table 8), we observed that 5 out of 10 patient samples yielded signal intensities higher than normal range: Sample #1, 4, 5, 8, 10. Among them, Sample #1, 5, 10 were localized in the head of pancreas; and Sample #4 and 8 were from the body of the pancreas. Thus, we hypothesized that patient with pancreas located at the head of the pancreas might have higher level of serum CA19-9, and this would be our focus of future measurement and quantification. The "OVERFLW" indicated too high signal intensity due to excessive amount of CA19-9 in the sample. The existence of signal overflow directed us to determine the best working concentration range more carefully for CA19-9 measurement.

Samples	Sample_ Dilution	Dilution times	Sample ID
3.169			
0.412			
1.56	2.79	5X	RiceBao_1
4.027	2.056	10X	
OVRFLW	0.215	5X	RiceBao_2
1.834	0.14	10X	
1.105	0.719	5X	RiceBao_3
2.321	0.365	10X	
0.626			
3.311			

Table 8 Absorbance signal readouts of CA19-9 levels in ten patient serum samples

Left column corresponded to Sample 1-10 and in Samples #1, 2 and 3 with 5X and 10X dilutions.

We then moved on to measure mock pancreatic cancer patient serum samples to further validate our ILISA platform. Mock samples were created by adding human CA19-9 to pooled human serum at designated concentration. Measurement results displayed great linearity (Figure 43).

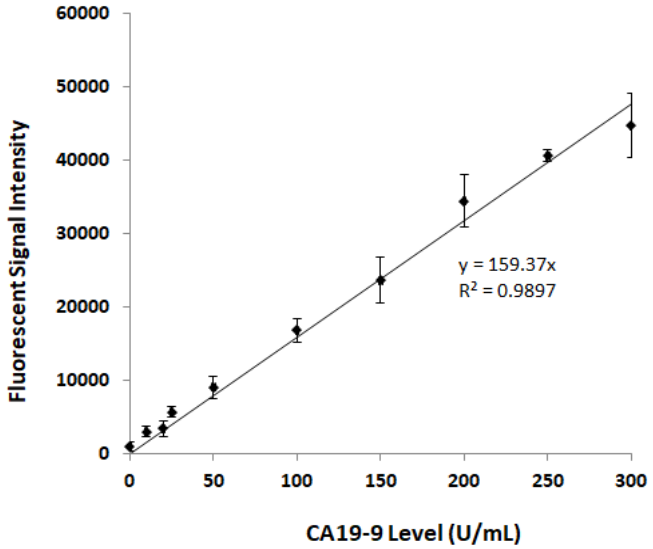

Figure 43 Measurement of mock samples

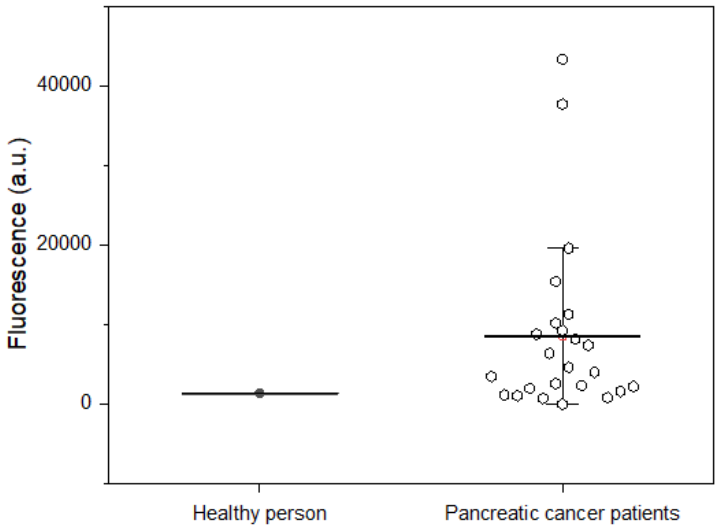

Figure 44 Results of CA19-9 in pancreatic cancer patient sera

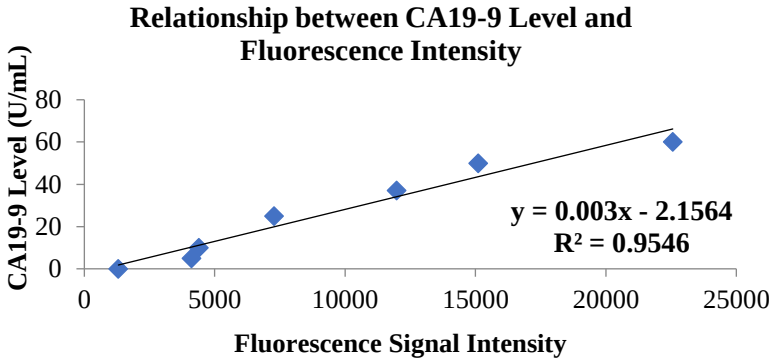

Figure 45 Relationship between CA19-9 level and fluorescence intensity

We picked a total of 24 patient serum samples for measurement (Figure 44). Compared with pooled serum from healthy people which yielded very low fluorescence signal intensity, the patient serum samples on average yielded higher signal intensity. The range of CA19-9 levels in cancer patients could also be very large and it could be successfully covered by our ILISA measurement with a wide dynamic range. The CA19-9 levels in patient serum samples were back calculated (Table 9) based on the fluorescence signal intensities measured and the standard curve obtained as shown in Figure 45.

ID Label	CA19-9 (U/mL)	ID Label	CA19-9 (U/mL)	ID Label	CA19-9 (U/mL)	ID Label	CA19-9 (U/mL)
S1	58.9	**S18**	286.0	**S24**	12.7	**S30**	142.8
S2	27.7	**S19**	85.4	**S25**	222.7	**S31**	5.9
S3	24.4	**S20**	18.4	**S26**	113.0	**S32**	560.7
S4	128.7	**S21**	-11.4	**S27**	646.8	**S33**	101.0
S15	-0.7	**S22**	1.0	**S28**	122.0	**S34**	21.8
S16	49.2	**S23**	4.5	**S29**	159.8	**S35**	40.9

Table 9 Calculated values of CA19-9 levels (U/mL) of the 24 patient serum samples examined

4.2.4 Conclusion

We confirmed that ILISA with Eu_xFe_yO NP probes accurately and sensitively quantified the CA19-9 levels in healthy and diseased serum samples and can be used to differentiate healthy and cancer patients.

4.2.5 Future Work

To obtain a more statistically meaningful analysis of the relationship between biomarker levels and patient conditions, power analysis should be exploited to determine how many patient serum samples will be needed, taking into considerations of all patient characteristics for stratification, especially the stages of the disease.

It is worth noting that none of these tumor marker tests is regarded as the gold standard for diagnosis purpose in clinical practice due to not high enough accuracy to determine if someone has pancreatic cancer[139]. Not every patient with confirmed diagnosis of pancreatic cancer has high levels of these markers, and some people without pancreatic cancers might have elevated levels of these markers for other reasons, such as other pancreatic diseases. Nevertheless, these tests can facilitate other tests in diagnosing pancreatic cancers. Researches have also suggested that parallel combination test of CA19-9 together with CA242 could offer better diagnostic value than

individual CA242 or CA19-9 test[131,138,140]. The ILISA platform with can be readily adapted to measuring CA242 with matched antibody pairs for capture and detection. With the improved detection limit, ILISA can enhance the specificity, accuracy and efficiency for diagnosis and screening.

4.3 To improve sensitivity and detection limit of ILISA

4.3.1 Experimental Design

We observed that the ILISA measurement showed low sensitivity in lower concentration ranges, indicated by the consistent up-drifting pattern of the standard curve (Figure 46). The up-drifting pattern in the lower concentration range mostly like resulted from unwanted high background signals, which might be due to incomplete washing of unbound nanoparticles. To push the limit of the detection, we tried to optimize several assay parameters and experimental procedures.

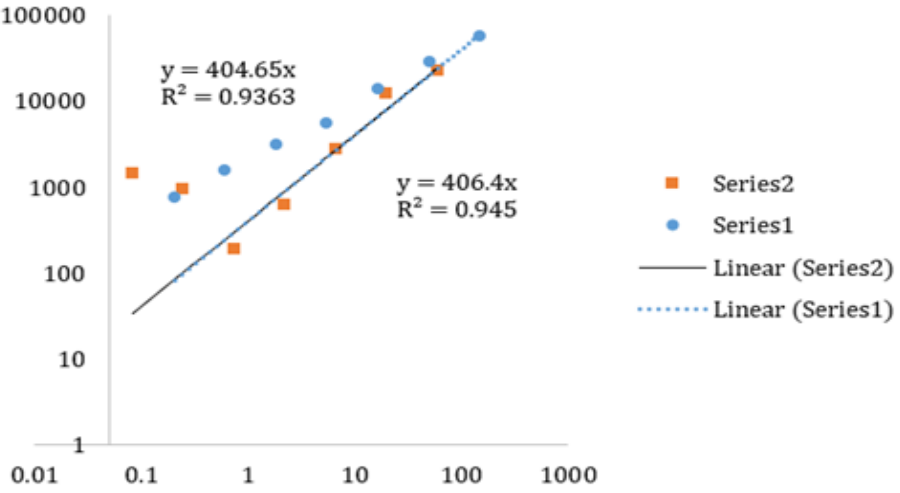

Figure 46 The up-drifting pattern of the standard curve

To achieve optimal fluorescent signal measurement using TECAN SPARK plate reader, we tried to optimize several parameters, including the gain (assigned value automatically generated by the reader, detonated as "Optimal" and manually set value), the reading positions (from the top or the bottom of the plate), types of the blocking proteins on the substrate, different plates with different autofluorescence, plate reader filters, incubation time, pH, washing steps and washing buffer concentrations and so on.

4.3.1 Materials and Methods

Several types of blocking proteins were prepared: 3% BSA, 3% BSA filtered after mixing by a 0.2μm filter, 3% BSA centrifuged at 500G for 1min, 5% BSA, and 5% milk (N = 4).

Complete randomization or rotation randomization were adopted when assigning samples of serial dilutions to each well. Strips from newly

opened plate and old strips were also tested again each other to eliminate artifacts (Figure 47).

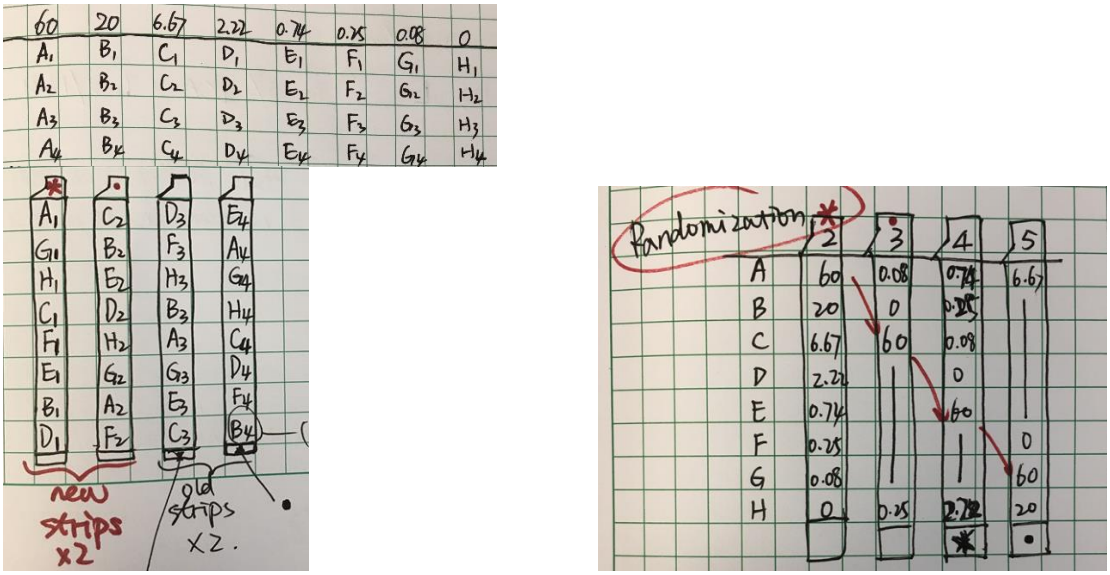

Figure 47 Complete randomization (left) or rotation randomization (right) for sample assignments

4.3.2 Results and Discussions

First, we tested whether the blocking proteins played a role in reducing background signals. We teste several choices of blocking proteins that have been commonly used for developing ELISA (Figure 48). The signal intensity of the blocking protein should be as low as possible to yield better signals from the successfully bound nanoparticles. We still used 3% BSA (no centrifuge) for later experiments.

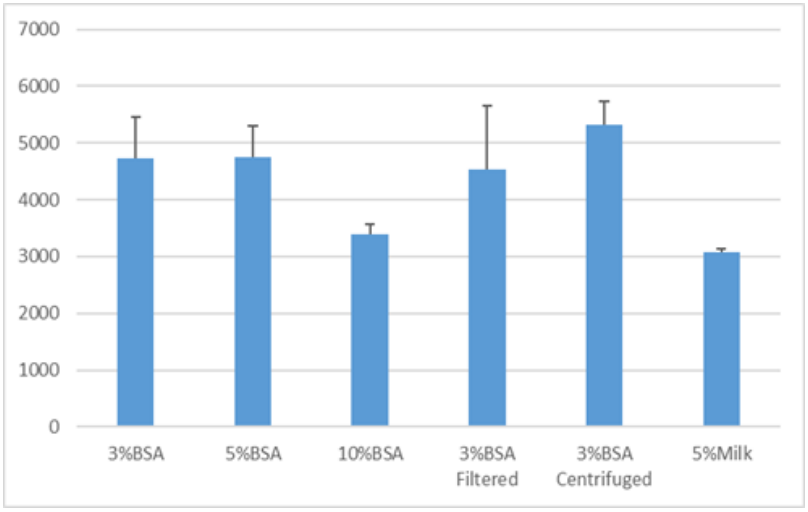

Figure 48 Background signal intensities from various blocking proteins

We next evaluate the effect of incubation time. According to kit manual, the incubation time was set to 2.5 hours after adding standard protein. We tried to change to 1 hour of incubation after adding standard protein and observed no defined influence on standard curve caused by different incubation time (Figure 49).

• **1 hour incubation** after adding standard protein

Read Position	Top		Bottom	
Gain	Manual - 120	Optimal - 146	Manual - 120	Optimal - 194
Standard Curve & Plot	y = 121.19x R^2 = 0.9957 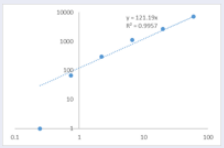	y = 581.87x R^2 = 0.9926 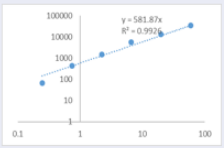	y = 3.9183x R^2 = 0.9859 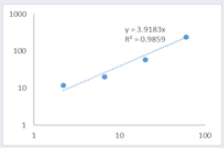	y = 190.69x R^2 = 0.9954 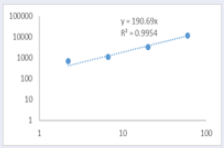
Plot w/ deletion of outlier data points	y = 121.21x R^2 = 0.9957 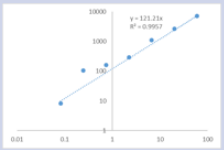	y = 583.49x R^2 = 0.9927 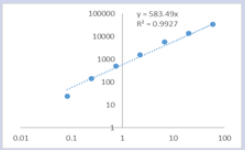	y = 4.0807x R^2 = 0.9882 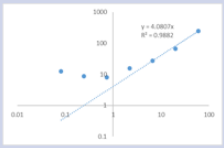	y = 201.02x R^2 = 0.9944 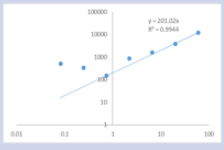

• **2.5 hours incubation** after adding standard protein

Read Position	Top			Bottom	
Gain	Manual - 120	Manual - 130	Optimal - 149	Manual - 120	Optimal - 197
Standard Curve & Plot (N=4)	y = 97.721x R^2 = 0.9645 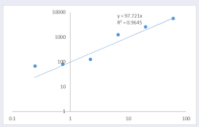	y = 199.98x R^2 = 0.9485 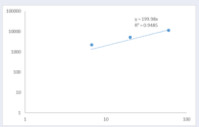	y = 549.32x R^2 = 0.9129 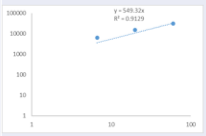	y = 2.3914x R^2 = 0.8751 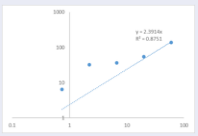	y = 549.32x R^2 = 0.9129 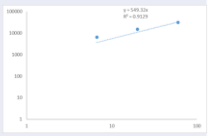
Plot w/ deletion of outlier data points (N≥3)	(N/A)	y = 214.28x R^2 = 0.9729 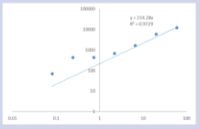	y = 590.93x R^2 = 0.961 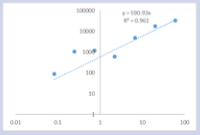	y = 2.7647x R^2 = 0.8754 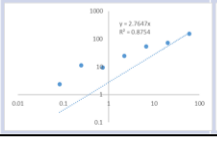	y = 598.29x R^2 = 0.9283 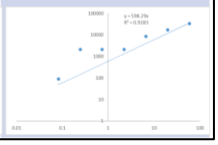

Figure 49 Comparison of readout results of different incubation times

We also confirmed that pH change induced no difference based on the result that adding 1M NaOH did not change readouts (data not shown).

For assessing randomization of well assignment to minimizing artifact due to manual operation or quality of the well coating, two strips from older

kit and two strips from newly opened kit. There was no significant change in measurement of signal intensities (Figure 50).

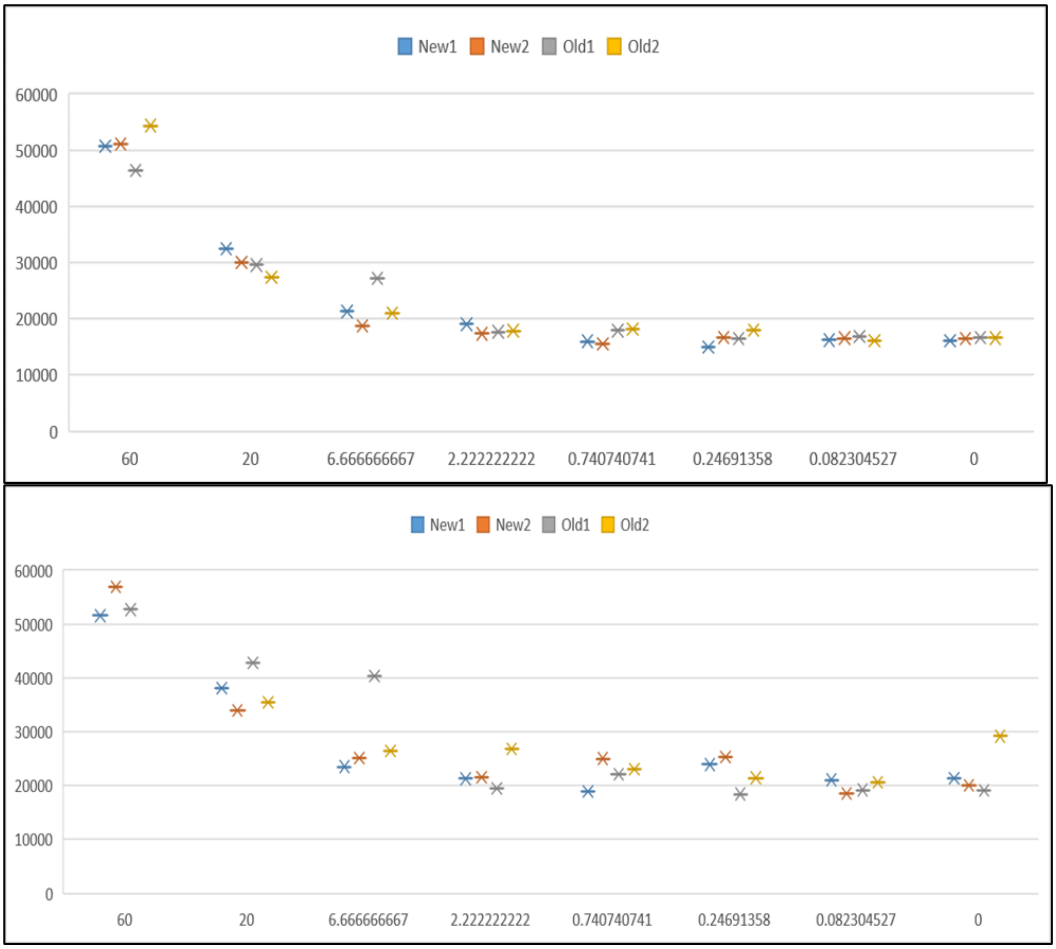

Figure 50 Comparison of readout results between old and new strips from different plates/kits with the same lot number

We also tried to adjust the concentrations of components in the washing buffer (Figure 51) and assumed rigorous washing steps by both manual decanting process and by plate washing machine. Increasing the Tween concentration from 0.5% to 1% suggested possible improvement on diminishing background signals as indicated by the decreased slope.

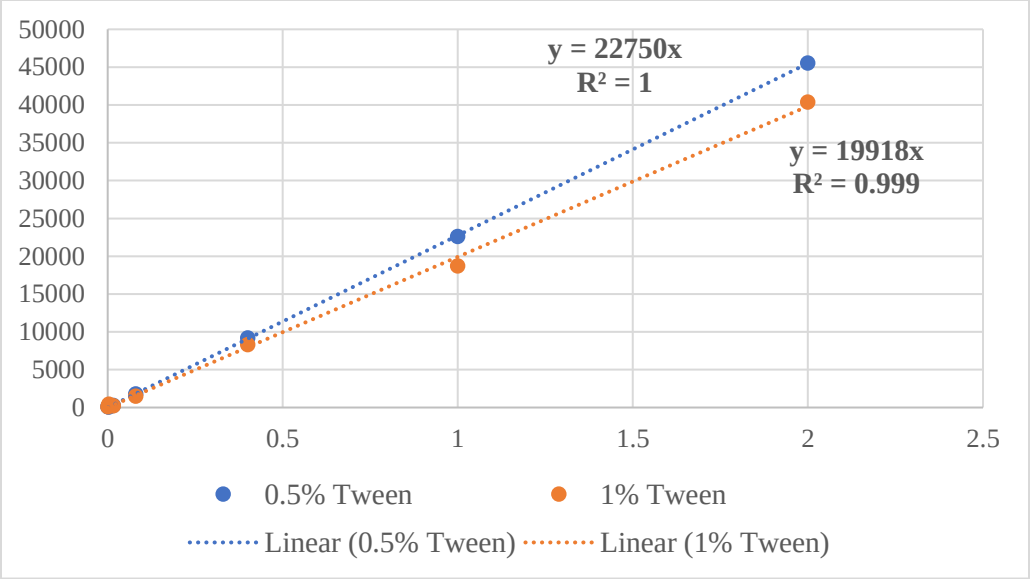

Figure 51 Effect of Tween concentration in washing buffer on signal intensity

4.3.3 Conclusion

We explored the effects of various parameters on reducing the background signal of the ILISA platform. However, limited improvement was achieved. A theoretical detection limit should be investigated.

4.3.4 Future Work

To further improve the detection limit, we might try to translate from solid phase immunoassay to liquid phase using Eu_xFe_yO NPs like magnetic bead immunoassay. Integrated with centrifugation process, the magnetic properties of the Eu_xFe_yO NPs might help remove unbound free nanoparticles to minimize background signal.

The ILISA platform presents potential for multiplexed testing for a panel of biomarkers collectively or to quantify multiple types of proteins at the single-cell level. Different biomarkers show distinct levels under normal and diseased conditions. Given the large dynamic range of the ILISA technology, they can be measured together and be distinguished from each other.

Multiplexing may be achieved by:

1) subdividing one serum sample into smaller portions for analysis. Given the high sensitivity and enhanced detection limit, ILISA requires minimal usage of samples for each detection. It would be extremely beneficial to get detection limit down to single-cell protein level for potential personalized oncology biomarker analysis.

2) using different rare-earth elements (for example, lanthanum) for doping in MIONs plus different antibody conjugations. In this way, different peaks under different wavelengths of lasers can be completed in one readout. Fluorophores with distinct excitation/emission peaks or quantum dots may help expand the types of analytes to be measured simultaneously.

3) designing different pull-down kinetics of antigens. Magnets may be deployed to better retain bound nanoparticles while washing away nonspecifically bound nanoparticles to minimize the background signal.

Potential applications of ILISA can also be extended to viral particle quantification or infection screening using serum samples[73]. Human IgG and IgM levels are elevated during viral infection and this may serve as the principle to develop assays for fast screening during a pandemic like COVID-19. Research also showed that type-I IFN deficiency in the blood could be a hallmark of severe COVID-19 and measuring key cytokines level which requires at 100-fold more sensitivity than conventional ELISA would provide a rationale for combined therapeutic approaches[141,142].

Conclusions

We employed magnetic iron oxide nanoparticles (MIONs) for three biomedical applications, taking advantages of the unique magnetic properties of MIONs. We adopted cell penetrating peptide conjugation onto MIONs to increase endocytosis of MIONs into T cells. This enabled better *in vivo* imaging and targeting by magnetic force to improve the efficacy of cancer immunotherapy for solid tumors. We coated MIONs with mesoporous silica and demonstrated enhanced colloidal stability and heating efficiency. This formulation could be used to facilitate hyperthermia therapy and anticancer drug delivery by heat-triggered release. We quantified pancreatic cancer biomarkers in patient serum samples using europium-doped iron oxide nanoparticle-linked immunosorbent assay (ILISA). The detection limit of ILISA could be further optimized to measure the levels of trace biomarkers for early cancer detection with high sensitivity. Our work further expanded the translational potentials of MIONs to revolutionize current clinical diagnostic and therapeutic techniques.

References

1. Tong, S., Zhu, H. & Bao, G. Magnetic iron oxide nanoparticles for disease detection and therapy. *Mater. Today* (2019) doi:10.1016/J.MATTOD.2019.06.003.
2. Laurent, S. *et al.* Magnetic iron oxide nanoparticles: Synthesis, stabilization, vectorization, physicochemical characterizations and biological applications. *Chem. Rev.* **108**, 2064–2110 (2008).
3. Wu, W., He, Q. & Jiang, C. Magnetic iron oxide nanoparticles: Synthesis and surface functionalization strategies. *Nanoscale Res. Lett.* **3**, 397–415 (2008).
4. Tong, S., Quinto, C. A., Zhang, L., Mohindra, P. & Bao, G. Size-Dependent Heating of Magnetic Iron Oxide Nanoparticles. *ACS Nano* **11**, 6808–6816 (2017).
5. Tong, S., Hou, S., Ren, B., Zheng, Z. & Bao, G. Self-assembly of phospholipid-PEG coating on nanoparticles through dual solvent exchange. *Nano Lett.* **11**, 3720–3726 (2011).
6. Berry, C. C. & G Curtis, A. S. Functionalisation of magnetic nanoparticles for applications in biomedicine. *J. Phys. D. Appl. Phys.* **36**, 198–206 (2003).
7. Krishnan, K. M. *et al.* Nanomagnetism and spin electronics: Materials, microstructure and novel properties. *J. Mater. Sci.* **41**, 793–815 (2006).
8. Bonnemain, B. Superparamagnetic agents in magnetic resonance imaging: Physicochemical characteristics and clinical applications. A review. *Journal of Drug Targeting* vol. 6 167–174 (1998).
9. Wang, Y. X. J., Hussain, S. M. & Krestin, G. P. Superparamagnetic iron oxide contrast agents: Physicochemical characteristics and applications in MR imaging. *Eur. Radiol.* **11**, 2319–2331 (2001).
10. Gleich, B. & Weizenecker, J. Tomographic imaging using the nonlinear response of magnetic particles. *Nature* **435**, 1214–1217 (2005).
11. Tong, S., Hou, S., Zheng, Z., Zhou, J. & Bao, G. Coating optimization of superparamagnetic iron oxide nanoparticles for high T2 relaxivity. *Nano Lett.* **10**, 4607–4613 (2010).
12. Lee, J. H. *et al.* Artificially engineered magnetic nanoparticles for ultra-sensitive molecular imaging. *Nat. Med.* (2007) doi:10.1038/nm1467.
13. Jang, J. T. *et al.* Critical enhancements of MRI contrast and hyperthermic effects by dopant-controlled magnetic nanoparticles. *Angew. Chemie - Int. Ed.* (2009) doi:10.1002/anie.200805149.
14. Lee, N. *et al.* Iron Oxide Based Nanoparticles for Multimodal Imaging and Magnetoresponsive Therapy. *Chemical Reviews* vol. 115 10637–10689 (2015).
15. Bao, G., Mitragotri, S. & Tong, S. Multifunctional Nanoparticles for Drug Delivery and Molecular Imaging. *Annu. Rev. Biomed. Eng.* **15**, 253–282 (2013).
16. Ma, Y., Tong, S., Bao, G., Gao, C. & Dai, Z. Indocyanine green loaded SPIO nanoparticles with phospholipid-PEG coating for dual-modal imaging and photothermal therapy. *Biomaterials* (2013) doi:10.1016/j.biomaterials.2013.07.007.
17. Jain, T. K., Reddy, M. K., Morales, M. A., Leslie-Pelecky, D. L. & Labhasetwar,

V. Biodistribution, clearance, and biocompatibility of iron oxide magnetic nanoparticles in rats. *Mol. Pharm.* **5**, 316–327 (2008).
18. Reddy, L. H., Arias, J. L., Nicolas, J. & Couvreur, P. Magnetic nanoparticles: Design and characterization, toxicity and biocompatibility, pharmaceutical and biomedical applications. *Chemical Reviews* vol. 112 5818–5878 (2012).
19. Mahmoudi, M., Hofmann, H., Rothen-Rutishauser, B. & Petri-Fink, A. Assessing the in vitro and in vivo toxicity of superparamagnetic iron oxide nanoparticles. *Chemical Reviews* vol. 112 2323–2338 (2012).
20. Arami, H., Khandhar, A., Liggitt, D. & Krishnan, K. M. In vivo delivery, pharmacokinetics, biodistribution and toxicity of iron oxide nanoparticles. *Chem. Soc. Rev.* **44**, 8576–8607 (2015).
21. Zhang, S., Gao, H. & Bao, G. Physical Principles of Nanoparticle Cellular Endocytosis. *ACS Nano* **9**, 8655–8671 (2015).
22. Schulze, E. *et al.* Cellular uptake and trafficking of a prototypical magnetic iron oxide label in vitro. *Invest. Radiol.* **30**, 604–610 (1995).
23. Weissleder, R. *et al.* Superparamagnetic iron oxide: Pharmacokinetics and toxicity. *Am. J. Roentgenol.* **152**, 167–173 (1989).
24. Bobo, D., Robinson, K. J., Islam, J., Thurecht, K. J. & Corrie, S. R. Nanoparticle-Based Medicines: A Review of FDA-Approved Materials and Clinical Trials to Date. *Pharmaceutical Research* vol. 33 2373–2387 (2016).
25. Bulte, J. W. M. In Vivo MRI Cell Tracking: Clinical Studies. *Am. J. Roentgenol.* **193**, 314–325 (2009).
26. Cerdan, S., Lötscher, H. R., Künnecke, B. & Seelig, J. Monoclonal antibody-coated magnetite particles as contrast agents in magnetic resonance imaging of tumors. *Magn. Reson. Med.* **12**, 151–163 (1989).
27. Sun, C., Sze, R. & Zhang, M. Folic acid-PEG conjugated superparamagnetic nanoparticles for targeted cellular uptake and detection by MRI. *J. Biomed. Mater. Res. - Part A* **78**, 550–557 (2006).
28. Tiefenauer, L. X., Kühne, G. & Andres, R. Y. Antibody-Magnetite Nanoparticles: In Vitro Characterization of a Potential Tumor-Specific Contrast Agent for Magnetic Resonance Imaging. *Bioconjug. Chem.* **4**, 347–352 (1993).
29. Harisinghani, M. G. *et al.* Noninvasive Detection of Clinically Occult Lymph-Node Metastases in Prostate Cancer. *N. Engl. J. Med.* **348**, 2491–2499 (2003).
30. Wilhelm, S. *et al.* Analysis of nanoparticle delivery to tumours. *Nat. Rev. Mater.* **1**, 16014 (2016).
31. Liu, Y. *et al.* Transcytosis of Nanomedicine for Tumor Penetration. *Nano Lett.* acs.nanolett.9b03211 (2019) doi:10.1021/acs.nanolett.9b03211.
32. Lázaro, I. de & Mooney, D. J. A nanoparticle's pathway into tumours. *Nat. Mater. 2020 195* **19**, 486–487 (2020).
33. Weissleder, R., Cheng, H.-C., Bogdanova, A. & Bogdanov, A. Magnetically labeled cells can be detected by MR imaging. *J. Magn. Reson. Imaging* **7**, 258–263 (1997).
34. Yeh, T.-C., Zhang, W., Ildstad, S. T. & Ho, C. Intracellular labeling of T-cells with superparamagnetic contrast agents. *Magn. Reson. Med.* **30**, 617–625 (1993).
35. Yeh, T.-C., Zhang, W., Ildstad, S. T. & Ho, C. In Vivo Dynamic MRI Tracking of Rat T-Cells Labeled with Superparamagnetic Iron-Oxide Particles. *Magn. Reson.*

Med. **33**, 200–208 (1995).
36. Bulte, J. W. *et al.* Tagging of T cells with superparamagnetic iron oxide: uptake kinetics and relaxometry. *Acad. Radiol.* **3 Suppl 2**, S301-3 (1996).
37. Dodd, S. J. *et al.* Detection of Single Mammalian Cells by High-Resolution Magnetic Resonance Imaging. *Biophys. J.* **76**, 103–109 (1999).
38. Lee Josephson, Ching-Hsuan Tung, Anna Moore, A. & Weissleder, R. High-Efficiency Intracellular Magnetic Labeling with Novel Superparamagnetic-Tat Peptide Conjugates. (1999) doi:10.1021/BC980125H.
39. Dodd, C. H. *et al.* Normal T-cell response and in vivo magnetic resonance imaging of T cells loaded with HIV transactivator-peptide-derived superparamagnetic nanoparticles. *J. Immunol. Methods* **256**, 89–105 (2001).
40. Kaufman, C. L. *et al.* Superparamagnetic iron oxide particles transactivator protein-fluorescein isothiocyanate particle labeling for in vivo magnetic resonance imaging detection of cell migration: uptake and durability. *Transplantation* **76**, 1043–1046 (2003).
41. Sundstrom, J. B. *et al.* Magnetic resonance imaging of activated proliferating rhesus macaque T cells labeled with superparamagnetic monocrystalline iron oxide nanoparticles. *J. Acquir. Immune Defic. Syndr.* **35**, 9–21 (2004).
42. Hu, D.-E., Kettunen, M. I. & Brindle, K. M. Monitoring T-lymphocyte trafficking in tumors undergoing immune rejection. *Magn. Reson. Med.* **54**, 1473–1479 (2005).
43. Liu, Z. & Li, Z. Molecular imaging in tracking tumor-specific Cytotoxic T Lymphocytes (CTLs). *Theranostics* vol. 4 990–1001 (2014).
44. Sharkey, J. *et al.* Functionalized superparamagnetic iron oxide nanoparticles provide highly efficient iron-labeling in macrophages for magnetic resonance–based detection in vivo. *Cytotherapy* **19**, 555–569 (2017).
45. Miao, X., Leng, X. & Zhang, Q. The current state of nanoparticle-induced macrophage polarization and reprogramming research. *International Journal of Molecular Sciences* vol. 18 336 (2017).
46. Ahrens, E. T., Feili-Hariri, M., Xu, H., Genove, G. & Morel, P. A. Receptor-mediated endocytosis of iron-oxide particles provides efficient labeling of dendritic cells for in vivo MR imaging. *Magn. Reson. Med.* **49**, 1006–1013 (2003).
47. Lewin, M. *et al.* Tat peptide-derivatized magnetic nanoparticles allow in vivo tracking and recovery of progenitor cells. *Nat. Biotechnol.* **18**, 410–414 (2000).
48. Hinds, K. A. *et al.* Highly efficient endosomal labeling of progenitor and stem cells with large magnetic particles allows magnetic resonance imaging of single cells. *Blood* **102**, 867–72 (2003).
49. Frank, J. A. *et al.* Clinically Applicable Labeling of Mammalian and Stem Cells by Combining Superparamagnetic Iron Oxides and Transfection Agents. *Radiology* **228**, 480–487 (2003).
50. Arbab, A. S. *et al.* Efficient magnetic cell labeling with protamine sulfate complexed to ferumoxides for cellular MRI. *Blood* **104**, 1217–23 (2004).
51. Wu, Y. L. *et al.* In situ labeling of immune cells with iron oxide particles: an approach to detect organ rejection by cellular MRI. *Proc. Natl. Acad. Sci. U. S. A.* **103**, 1852–7 (2006).
52. Bakhru, S. H. *et al.* Enhanced cellular uptake and long-term retention of chitosan-

modified iron-oxide nanoparticles for MRI-based cell tracking. *Int. J. Nanomedicine* **7**, 4613–4623 (2012).
53. Kievit, F. M. *et al.* PEI-PEG-chitosan-copolymer-coated iron oxide nanoparticles for safe gene delivery: Synthesis, complexation, and transfection. *Adv. Funct. Mater.* **19**, 2244–2251 (2009).
54. Namgung, R. *et al.* Hybrid superparamagnetic iron oxide nanoparticle-branched polyethylenimine magnetoplexes for gene transfection of vascular endothelial cells. *Biomaterials* **31**, 4204–4213 (2010).
55. Qiu, Y. *et al.* Magnetic forces enable controlled drug delivery by disrupting endothelial cell-cell junctions. *Nat. Commun.* **8**, 1–10 (2017).
56. Zhu, H. *et al.* Spatial control of in vivo CRISPR–Cas9 genome editing via nanomagnets. *Nat. Biomed. Eng.* **3**, 126–136 (2019).
57. Ibrahim Yildiz. Applications of magnetic nanoparticles in biomedical separation and purification in: Nanotechnology Reviews. *Nanotechnol. Rev.* **5**, (2015).
58. Landázuri, N. *et al.* Magnetic Targeting of Human Mesenchymal Stem Cells with Internalized Superparamagnetic Iron Oxide Nanoparticles. *Small* **9**, 4017–4026 (2013).
59. Muthana, M. *et al.* Directing cell therapy to anatomic target sites in vivo with magnetic resonance targeting. *Nat. Commun.* **6**, 1–11 (2015).
60. Rosensweig, R. E. Heating magnetic fluid with alternating magnetic field. *J. Magn. Magn. Mater.* **252**, 370–374 (2002).
61. Manuchehrabadi, N. & Bischof, J. C. Superparamagnetic Iron Oxide Nanoparticle Heating. (2012) doi:10.1201/b12983-5.
62. Mallory, M., Gogineni, E., Jones, G. C., Greer, L. & Simone, C. B. Therapeutic hyperthermia: The old, the new, and the upcoming. *Critical Reviews in Oncology/Hematology* vol. 97 56–64 (2016).
63. Wust, P. *et al.* Hyperthermia in combined treatment of cancer. *Lancet Oncology* vol. 3 487–497 (2002).
64. Johannsen, M. *et al.* Morbidity and quality of life during thermotherapy using magnetic nanoparticles in locally recurrent prostate cancer: Results of a prospective phase I trial. *Int. J. Hyperth.* **23**, 315–323 (2007).
65. Maier-Hauff, K. *et al.* Intracranial thermotherapy using magnetic nanoparticles combined with external beam radiotherapy: Results of a feasibility study on patients with glioblastoma multiforme. *J. Neurooncol.* **81**, 53–60 (2007).
66. Chatterjee, S. K. & Zetter, B. R. Cancer biomarkers: Knowing the present and predicting the future. *Future Oncology* vol. 1 37–50 (2005).
67. GOLD, P. & FREEDMAN, S. O. DEMONSTRATION OF TUMOR-SPECIFIC ANTIGENS IN HUMAN COLONIC CARCINOMATA BY IMMUNOLOGICAL TOLERANCE AND ABSORPTION TECHNIQUES. *J. Exp. Med.* **121**, 439–462 (1965).
68. Koprowski, H., Herlyn, M., Steplewski, Z. & Sears, H. F. Specific antigen in serum of patients with colon carcinoma. *Science (80-.).* **212**, 53–55 (1981).
69. B C Del Villano, S Brennan, P Brock, C Bucher, V Liu, M McClure, B Rake, S Space, B Westrick, H Schoemaker, V R Zurawski, J. Radioimmunometric assay for a monoclonal antibody-defined tumor marker, CA 19-9. *Clin. Chem.* **29**, 549–552 (1983).

70. Yilmaz, A., Ece, F., Bayramgürler, B., Akkaya, E. & Baran, R. The value of Ca 125 in the evaluation of tuberculosis activity. *Respir. Med.* **95**, 666–669 (2001).
71. Barry, M. J. Prostate-Specific–Antigen Testing for Early Diagnosis of Prostate Cancer. *N. Engl. J. Med.* **344**, 1373–1377 (2001).
72. Tong, S., Ren, B., Zheng, Z., Shen, H. & Bao, G. Tiny grains give huge gains: Nanocrystal-based signal amplification for biomolecule detection. *ACS Nano* **7**, 5142–5150 (2013).
73. Zhang, L., Tong, S., Zhou, J. & Bao, G. Accurate quantification of disease markers in human serum using iron oxide nanoparticle-linked immunosorbent assay. *Theranostics* **6**, 1353–1361 (2016).
74. Adoptive Cell Therapy: CAR T, TCR, TIL, NK – Cancer Research Institute (CRI). https://www.cancerresearch.org/immunotherapy/treatment-types/adoptive-cell-therapy.
75. Definition of therapeutic tumor infiltrating lymphocytes - NCI Drug Dictionary - National Cancer Institute. https://www.cancer.gov/publications/dictionaries/cancer-drug/def/therapeutic-tumor-infiltrating-lymphocytes.
76. Definition of TCR-specific, alpha fetoprotein-enhanced autologous T lymphocytes - NCI Drug Dictionary - National Cancer Institute. https://www.cancer.gov/publications/dictionaries/cancer-drug/def/tcr-specific-alpha-fetoprotein-enhanced-autologous-t-lymphocytes.
77. CAR T-Cell Therapy Infographic - National Cancer Institute. https://www.cancer.gov/about-cancer/treatment/research/car-t-cell-therapy-infographic.
78. FDA approval brings first gene therapy to the United States | FDA. https://www.fda.gov/news-events/press-announcements/fda-approval-brings-first-gene-therapy-united-states.
79. FDA approves axicabtagene ciloleucel for large B-cell lymphoma | FDA. https://www.fda.gov/drugs/resources-information-approved-drugs/fda-approves-axicabtagene-ciloleucel-large-b-cell-lymphoma.
80. Guidotti, G., Brambilla, L. & Rossi, D. Cell-Penetrating Peptides: From Basic Research to Clinics. *Trends Pharmacol. Sci.* **38**, 406–424 (2017).
81. Moritz F. Kircher, Jennifer R. Allport, Edward E. Graves, Victoria Love, Lee Josephson, A. H. L. and R. W. & Romero, P. In Vivo High Resolution Three-Dimensional Imaging of Antigen-Specific Cytotoxic T-Lymphocyte Trafficking to Tumors. *Cancer Res.* **63**, 6838–6846 (2003).
82. Tang, H., Yin, L., Kim, K. H. & Cheng, J. Helical Poly(arginine) Mimics with Superior Cell-Penetrating and Molecular Transporting Properties. *Chem. Sci.* **4**, 3839–3844 (2013).
83. Ghosh, S., Panja, P., Dalal, C. & Jana, N. R. Arginine-Terminated, Chemically Designed Nanoparticle for Direct Cell Translocation. *ACS Appl. Bio Mater.* **2**, 339–348 (2019).
84. Riemer, J., Hoepken, H. H., Czerwinska, H., Robinson, S. R. & Dringen, R. Colorimetric ferrozine-based assay for the quantitation of iron in cultured cells. *Anal. Biochem.* **331**, 370–375 (2004).
85. (No Title).

https://docs.abcam.com/pdf/immunology/t_cells_the_usual_subsets.pdf.
86. Rosenbluth, M. J., Lam, W. A. & Fletcher, D. A. Force microscopy of nonadherent cells: A comparison of leukemia cell deformability. *Biophys. J.* **90**, 2994–3003 (2006).
87. Souza, G. R. *et al.* Three-dimensional tissue culture based on magnetic cell levitation. *Nat. Nanotechnol.* **5**, 291–296 (2010).
88. Connell, J. J., Patrick, P. S., Yu, Y., Lythgoe, M. F. & Kalber, T. L. Advanced cell therapies: Targeting, tracking and actuation of cells with magnetic particles. *Regen. Med.* **10**, 757–772 (2015).
89. Sanz-Ortega, L. *et al.* T cells loaded with magnetic nanoparticles are retained in peripheral lymph nodes by the application of a magnetic field. *J. Nanobiotechnology* **17**, (2019).
90. Mohseni, M. J. *et al.* Scalable magnet geometries enhance tumour targeting of magnetic nano-carriers. *Mater. Des.* 108610 (2020) doi:10.1016/j.matdes.2020.108610.
91. Pai, A. *et al.* Dynamically Programmable Magnetic Fields for Controlled Movement of Cells Loaded with Iron Oxide Nanoparticles. *ACS Appl. Bio Mater.* acsabm.0c00226 (2020) doi:10.1021/acsabm.0c00226.
92. Davenport, A. J. *et al.* CAR-T cells inflict sequential killing of multiple tumor target cells. *Cancer Immunol. Res.* **3**, 483–494 (2015).
93. Mulazzani, M. *et al.* Long-term in vivo microscopy of CAR T cell dynamics during eradication of CNS lymphoma in mice. *Proc. Natl. Acad. Sci. U. S. A.* **116**, 24275–24284 (2019).
94. Abastado, J. P. The next challenge in cancer immunotherapy: Controlling T-cell traffic to the tumor. *Cancer Research* vol. 72 2159–2161 (2012).
95. Werb, Z. & Lu, P. The Role of Stroma in Tumor Development. *Cancer Journal (United States)* vol. 21 250–253 (2015).
96. Adusumilli, P. S. *et al.* Regional delivery of mesothelin-targeted CAR T cell therapy generates potent and long-lasting CD4-dependent tumor immunity. *Sci. Transl. Med.* **6**, 261ra151-261ra151 (2014).
97. Katz, S. C. *et al.* Regional CAR-T cell infusions for peritoneal carcinomatosis are superior to systemic delivery. *Cancer Gene Ther.* **23**, 142–148 (2016).
98. Donovan, L. K. *et al.* Locoregional delivery of CAR T cells to the cerebrospinal fluid for treatment of metastatic medulloblastoma and ependymoma. *Nat. Med.* 1–12 (2020) doi:10.1038/s41591-020-0827-2.
99. Theruvath, J. *et al.* Locoregionally administered B7-H3-targeted CAR T cells for treatment of atypical teratoid/rhabdoid tumors. *Nat. Med.* 1–8 (2020) doi:10.1038/s41591-020-0821-8.
100. Tchou, J. *et al.* Safety and efficacy of intratumoral injections of chimeric antigen receptor (CAR) T cells in metastatic breast cancer. *Cancer Immunol. Res.* **5**, 1152–1161 (2017).
101. Lei, K. & Tang, L. Surgery-free injectable macroscale biomaterials for local cancer immunotherapy. *Biomaterials Science* vol. 7 733–749 (2019).
102. Coon, M. E., Stephan, S. B., Gupta, V., Kealey, C. P. & Stephan, M. T. Nitinol thin films functionalized with CAR-T cells for the treatment of solid tumours. *Nat. Biomed. Eng.* (2019) doi:10.1038/s41551-019-0486-0.

103. Titov, A. *et al.* Advancing CAR T-cell therapy for solid tumors: Lessons learned from lymphoma treatment. *Cancers* vol. 12 125 (2020).
104. Mardiana, S., Solomon, B. J., Darcy, P. K. & Beavis, P. A. Supercharging adoptive T cell therapy to overcome solid tumor–induced immunosuppression. *Sci. Transl. Med.* **11**, eaaw2293 (2019).
105. Binnewies, M. *et al.* Understanding the tumor immune microenvironment (TIME) for effective therapy. *Nat. Med.* **24**, 541–550 (2018).
106. Stylianopoulos, T., Munn, L. L. & Jain, R. K. Reengineering the Physical Microenvironment of Tumors to Improve Drug Delivery and Efficacy: From Mathematical Modeling to Bench to Bedside. *Trends in Cancer* **4**, 292–319 (2018).
107. Saeed, M., Gao, J., Shi, Y., Lammers, T. & Yu, H. Engineering nanoparticles to reprogram the tumor immune microenvironment for improved cancer immunotherapy. *Theranostics* **9**, 7981–8000 (2019).
108. Musetti, S. & Huang, L. Nanoparticle-Mediated Remodeling of the Tumor Microenvironment to Enhance Immunotherapy. *ACS Nano* acsnano.8b05893 (2018) doi:10.1021/acsnano.8b05893.
109. Chen, P. M. *et al.* Modulation of tumor microenvironment using a TLR-7/8 agonist-loaded nanoparticle system that exerts low-temperature hyperthermia and immunotherapy for in situ cancer vaccination. *Biomaterials* (2019) doi:10.1016/j.biomaterials.2019.119629.
110. Goebeler, M.-E. & Bargou, R. C. T cell-engaging therapies — BiTEs and beyond. *Nat. Rev. Clin. Oncol.* 1–17 (2020) doi:10.1038/s41571-020-0347-5.
111. Knežević, N. & Durand, J. O. Large pore mesoporous silica nanomaterials for application in delivery of biomolecules. *Nanoscale* **7**, 2199–2209 (2015).
112. Moller, K. & Bein, T. Inclusion Chemistry in Periodic Mesoporous Hosts. *Chemistry of Materials* vol. 10 2950–2963 (1998).
113. Xu, C., Lei, C. & Yu, C. Mesoporous silica nanoparticles for protein protection and delivery. *Frontiers in Chemistry* vol. 7 290 (2019).
114. Yi, D. K., Lee, S. S., Papaefthymiou, G. C. & Ying, J. Y. Nanoparticle architectures templated by SiO 2/Fe 2O 3 nanocomposites. *Chem. Mater.* **18**, 614–619 (2006).
115. Kim, J. *et al.* Multifunctional uniform nanoparticles composed of a magnetite nanocrystal core and a mesoporous silica shell for magnetic resonance and fluorescence imaging and for drug delivery. *Angew. Chemie - Int. Ed.* **47**, 8438–8441 (2008).
116. Ye, F. *et al.* Uniform mesoporous silica coated iron oxide nanoparticles as a highly efficient, nontoxic MRI T2 contrast agent with tunable proton relaxivities. *Contrast Media Mol. Imaging* **7**, 460–468 (2012).
117. Ding, H. L. *et al.* Fe3O4@SiO2 core/shell nanoparticles: The silica coating regulations with a single core for different core sizes and shell thicknesses. *Chem. Mater.* **24**, 4572–4580 (2012).
118. Nyalosaso, J. L. *et al.* Synthesis, decoration, and cellular effects of magnetic mesoporous silica nanoparticles. *RSC Adv.* **6**, 57275–57283 (2016).
119. López, V. *et al.* Janus Mesoporous Silica Nanoparticles for Dual Targeting of Tumor Cells and Mitochondria. *ACS Appl. Mater. Interfaces* **9**, 26697–26706

(2017).
120. Croissant, J. G., Fatieiev, Y. & Khashab, N. M. Degradability and Clearance of Silicon, Organosilica, Silsesquioxane, Silica Mixed Oxide, and Mesoporous Silica Nanoparticles. *Adv. Mater.* **29**, 1604634 (2017).
121. Perton, F. *et al.* Fluorescent and magnetic stellate mesoporous silica for bimodal imaging and magnetic hyperthermia. *Appl. Mater. Today* **16**, 301–314 (2019).
122. Krishna, M. C. *et al.* Hyperthermic sensitization by the radical initiator 2,2'azobis (2-amidinopropane) dihydrochloride (AAPH). I. In vitro studies. *Int. J. Hyperth.* **10**, 271–281 (1994).
123. Aggarwal, P., Hall, J. B., McLeland, C. B., Dobrovolskaia, M. A. & McNeil, S. E. Nanoparticle interaction with plasma proteins as it relates to particle biodistribution, biocompatibility and therapeutic efficacy. *Advanced Drug Delivery Reviews* vol. 61 428–437 (2009).
124. Hadjidemetriou, M. & Kostarelos, K. Nanomedicine: Evolution of the nanoparticle corona. *Nat. Nanotechnol.* **12**, 288–290 (2017).
125. Hurley, K. R. *et al.* Predictable heating and positive MRI contrast from a mesoporous silica-coated iron oxide nanoparticle. *Mol. Pharm.* **13**, 2172–2183 (2016).
126. Manuchehrabadi, N. *et al.* Improved tissue cryopreservation using inductive heating of magnetic nanoparticles. *Sci. Transl. Med.* **9**, eaah4586 (2017).
127. Gao, Z. *et al.* Preparation of Scalable Silica-Coated Iron Oxide Nanoparticles for Nanowarming. *Adv. Sci.* **7**, 1901624 (2020).
128. Common Cancer Types - National Cancer Institute. https://www.cancer.gov/types/common-cancers.
129. O'Brien, D. P. *et al.* Serum CA19-9 is significantly upregulated up to 2 years before diagnosis with pancreatic cancer: Implications for early disease detection. *Clin. Cancer Res.* **21**, 622–631 (2015).
130. E. Poruk, K. *et al.* The Clinical Utility of CA 19-9 in Pancreatic Adenocarcinoma: Diagnostic and Prognostic Updates. *Curr. Mol. Med.* **13**, 340–351 (2013).
131. Gui, J.-C., Yan, W.-L. & Liu, X.-D. CA19-9 and CA242 as tumor markers for the diagnosis of pancreatic cancer: a meta-analysis. *Clin. Exp. Med.* **14**, 225–33 (2014).
132. Bao, G. & Tong, S. Nanocrystal Based Biomolecule Detection. (2013).
133. E Soini, I. H. Fluoroimmunoassay: present status and key problems. *Clin. Chem.* **25**, 353–361 (1979).
134. Siitari, H., Hemmilä, I., Soini, E., Lövgren, T. & Koistinen, V. Detection of hepatitis B surface antigen using time-resolved fluoroimmunoassay. *Nature* **301**, 258–260 (1983).
135. Hä, H., Soukka, T. & Lö, T. *Europium Nanoparticles and Time-resolved Fluorescence for Ultrasensitive Detection of Prostate-specific Antigen*. https://academic.oup.com/clinchem/article-abstract/47/3/561/5639498 (2001).
136. Diamandis, E. P. Time-resolved fluorometry in nucleic acid hybridization and Western blotting techniques. *Electrophoresis* **14**, 866–875 (1993).
137. User Guide: TCEP HCl. https://www.thermofisher.com/document-connect/document-connect.html?url=https%3A%2F%2Fassets.thermofisher.com%2FTFS-

Assets%2FLSG%2Fmanuals%2FMAN0011306_TCEP_HCl_UG.pdf&title=VXNlciBHdWlkZTogIFRDRVAgSENs.
138. Zhang, Y. *et al.* Tumor markers CA19-9, CA242 and CEA in the diagnosis of pancreatic cancer: A meta-analysis. *International Journal of Clinical and Experimental Medicine* vol. 8 11683–11691 (2015).
139. Tests for Pancreatic Cancer. https://www.cancer.org/cancer/pancreatic-cancer/detection-diagnosis-staging/how-diagnosed.html.
140. Ni, X. G. *et al.* The clinical value of serum CEA, CA19-9, and CA242 in the diagnosis and prognosis of pancreatic cancer. *Eur. J. Surg. Oncol.* **31**, 164–169 (2005).
141. Acharya, D., Liu, G. & Gack, M. U. Dysregulation of type I interferon responses in COVID-19. *Nat. Rev. Immunol.* 1–2 (2020) doi:10.1038/s41577-020-0346-x.
142. Blanco-Melo, D. *et al.* Imbalanced Host Response to SARS-CoV-2 Drives Development of COVID-19. *Cell* (2020) doi:10.1016/j.cell.2020.04.026.

Appendix

III. Protocol for Synthesis of Fe_3O_4@MS nanoparticles

This protocol was modified based on Ref[118].

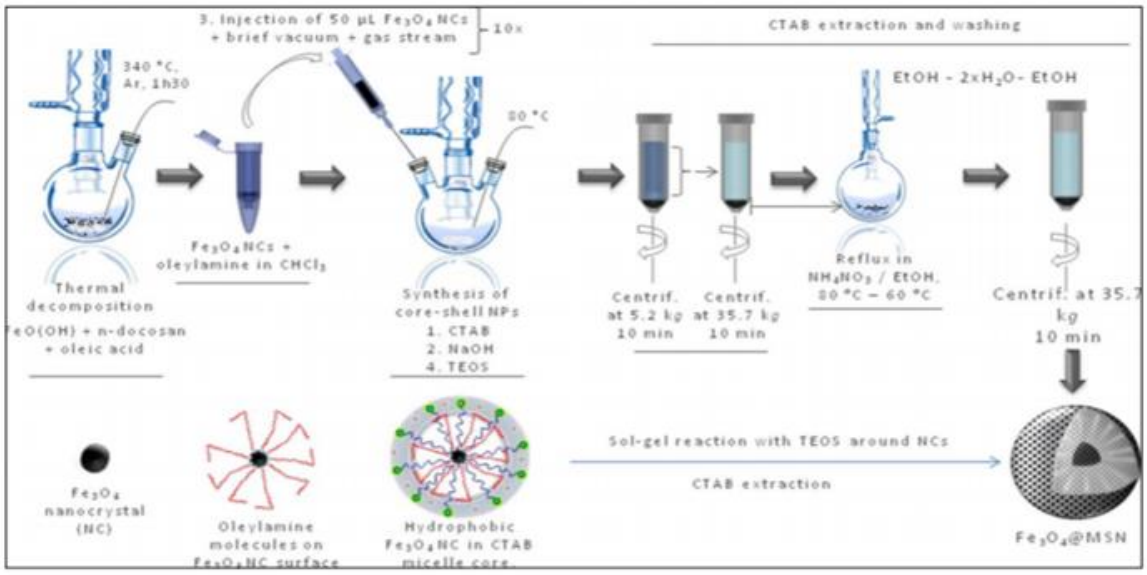

SI1: Scheme of each step of the synthesis, from Fe_3O_4 magnetic iron oxide nanocrystals (MIONs) to native core shell Fe_3O_4@MSN.

	Catalog #	Purity	MW (mg/mmol)	Moles	Volume	Mass
D_{20nm} Iron Oxide Nanoparticle (~3.19 mg/mL)					1.53 ml	
Hexadecyltrimethylammonium bromide (HTAB)	H5882 SIGMA	≥98%	364.45	0.343mmol		125mg
Tetraethyl orthosilicate (TEOS)	131903 ALDRICH	98%	208.33		0.1 mL + 0.5 mL	
NaOH			40	0.88mmol		35.2mg

1. 125 mg of CTAB in a 250 mL three-necked round bottom flask containing 60 g of ultrapure water and 0.44 mL of a solution of NaOH (2 M) (35.2mg NaOH).
2. This micellar solution was then heated to 70 °C under vigorous stirring (750 rpm) for 1 hour stabilization.
3. 1.53 mL of the suspension of MIONs, previously dispersed with ultrasonics for 3h, was injected stepwise (10 x 50 µL) into the micelle solution during 50 minutes. Between each injection, a partial and brief vacuum of 2 seconds was

applied followed by a gas stream (Ar or air) in order to remove the chloroform (MIONs solvent) from the micellar solution.

4. Following these injections, the reaction mixture was heated to 80 °C. At this temperature, a vacuum was one more time applied briefly followed by a gas stream. This was repeated once again before leaving the reaction mixture to stabilize under stirring for 1 hour at 80 °C.
5. An initial amount of 0.1 mL of TEOS was added to the mixture. Keep 30 min of reaction.
6. An additional 0.5 mL of TEOS was added to complete the sol-gel reaction. The condensation process was conducted for 1h30min.
7. After reaction, the mixture was slowly cooled down at room temperature while stirring, and then collected in NalgeneTM tubes for centrifugation at 5,200 g (7.5 krpm) for 10 minutes. This first centrifugation at 5.2 kg was carried out in order to extract more dense multi-core silica particles that may be present in the sediment. Then, the supernatant was centrifuged a second time at 35,700 g (20 krpm) for 10 minutes in order to collect the solid.
8. To extract efficiently the surfactant from the NPs, the solid was re-dispersed in a 100 mL round flask containing 50 mL of an alcoholic solution of nitrate ammonium (6g/L in EtOH) and was refluxed at 80 ° C for 2 h, then at 60 ° C overnight. The sample was centrifuged at 35,700 g for 10 minutes and washed 4 times consecutively with 30 mL of EtOH, twice with water, then EtOH. Each washing step involved 15 minutes of sonication and a centrifugation operation at 35,700 g for 10 minutes. Finally, the sample was dried for 4 hours in vacuum at room temperature.

IV. Patient Serum Sample Information

Batch #	Original ID by MDACC	Labeling		Stage (N/A = Not availabl e at this time)	Locatio n in Pancrea s	Age at specimen collection	Race 1=White 2=Black or African-American 3=American Indian or Alaska Native 4=Asian 7=Native Hawaiian or other Pacific Islander 95=Other	Gender 1=Male 2=Femal e 99=Unk nown	Diagnos ed with diabete s? 0=No 1=Yes	Alcohol Use 0=No 1=Yes	Smokin g History 0=No 1=Yes
1	RiceBao_1	S1	RiceBao_1	IIB	Head	69	95	1	0	1	0
	RiceBao_8	S2	RiceBao_8	IIA	Head	71	1	1	1	1	1
	RiceBao_9	S3	RiceBao_9	IIB	Head	55	1	2	1	1	1
	RiceBao_10	S4	RiceBao_10	IIA	Head	60	1	1	0	1	1
2	167752-25	S15	1167752-25	IIA	Head	57	1	2	0	0	1
	1043556-25	S16	1043556-25	IIB	Head	52	1	2	0	0	1
	1044876-25	S18	1044876-25	IIB	Head	62	1	1	0	1	0
	1048068-25	S19	1048068-25	IIB	Head	57	1	1	1	0	1
	864392-25	S20	864392-25	IIB	Head	75	1	1	0	0	0
	902538-26	S21	902538-26	IIB	Head	69	1	1	0	1	1
	1061366-25	S22	1061366-25	IIB	Head	70	1	2	0	0	0
	1063488-25	S23	1063488-25	IIB	Head	59	1	1	0	0	0
	1130968-25	S24	1130968-25	IIB	Head	71	2	2	0	0	0
	922573-25	S25	922573-25	IIB	Head	60	1	1	1	1	0
	990876-25	S26	990876-25	IIB	Head	72	1	1	0	1	0
	998771-25	S27	998771-25	IIB	Head	68	1	1	0	1	1
	1014116-25	S28	1014116-25	IIB	Head	59	1	1	0	1	0
	1022764-25	S29	1022764-25	IIB	Head	71	1	1	1	0	0
	1029165-25	S30	1029165-25	IIB	Head	60	1	2	0	1	0
	334434-40	S31	334434-40	IIA	Head	59	1	2	0	0	1
	336011-40	S32	336011-40	IIA	Head	65	1	2	0	1	0
	842698-27	S33	842698-27	IIA	Head	51	95	2	0	1	0
	814334-27	S34	814334-27	IIB	Head	54	1	1	1	1	1
	780544-25	S35	780544-25	IIA	Head	58	1	1	0	1	0